J. Mech. Phys. Solids 159 (2022) 104752

Contents lists available at ScienceDirect

Journal of the Mechanics and Physics of Solids

journal homepage: www.elsevier.com/locate/jmps

A strain gradient brittle fracture model based on two-scale asymptotic analysis

Yipeng Rao [a,b], Meizhen Xiang [b,*], Junzhi Cui [a,*]

[a] LSEC, ICMSEC, Academy of Mathematics and Systems Sciences, CAS, Beijing, 100090, China
[b] Laboratory of Computational Physics, Institute of Applied Physics and Computational Mathematics, Beijing, 100088, China

ARTICLE INFO

Keywords:
Brittle fracture
Strain gradient
Griffith criterion
Asymptotic analysis

ABSTRACT

Based on a two-scale asymptotic analysis procedure, we rigorously derive a new macroscopic brittle fracture model for materials with micro-cracks inside. Strain gradient effects are naturally involved in the model in the absence of any phenomenological assumptions. Coefficients of the fracture criterion are expressed in form of derivatives of the fourth- and sixth-order effective elastic tensors that are explicitly related to solutions of the first order unit cell problems. The model is numerically implemented into a finite element code. Abilities of the model to predict microstructure size effects and strain gradient effects on macro fracture behaviors are confirmed by numerical simulations. The model is also validated against experimental measurements.

1. Introduction

Nonlocality is intrinsic in solid mechanical responses since deformation of solids is ultimately governed by nonlocal atomistic interactions. Mechanical behaviors of solid materials and structures also depend on microstructural morphology of typical microstructures (e.g., voids, defects, dislocations, grains and grain boundaries) at different scales. Classical continuum mechanics, which fundamentally assumes local dependence between stress and strain, can only be applicable in describing the overall behavior of materials if the largest of the microstructural lengths is much smaller than the scale of application (Peerlings and Fleck, 2004). When the relevant macroscopic length approaches the largest microstructural scale in a material, classical continuum mechanics fails to capture the significant scale effects related to microscale nonlocal interactions (Peerlings and Fleck, 2004; Smyshlyaev and Cherednichenko, 2000; Li, 2011; Li et al., 2011).

Driven by the needs to describe scale effects, generalized nonlocal continuum mechanics are promoted rapidly. For example, Eringen et al. relaxed the local assumption which is tacitly accepted in the constitutive equations of classical continuum mechanics (Eringen, 1972, 1974; Povstenko, 1999). Thus, the stress at a point is expressed by a volume integral of strain over a domain of finite size . The rapidly developing peridynamics theory also has a similar fundament, in which mechanical interactions depends on displacement field in a domain of finite size through volume integral (Silling et al., 2007; Han et al., 2016). Nonlocal models expressed in form of integrals are strong non-local models, which can be approximated by the strain gradient models where mechanical responses are related to higher-order gradients of strain. Comparing to the integral form strong nonlocal models, the strain gradient models may be viewed as having weak nonlocality. Strain-gradient elasticity was first developed by in 1960s (Toupin, 1962, 1964; Mindlin, 1965; Mindlin and Eshel, 1968). Since then, strain gradient elasticity has grained rapid development and wide application (see for example Ru and Aifantis (1993), Gutkin and Aifantis (2015), Aifantis (2003), Lazar and Po (2015)). In addition to pure elasticity theories, strain gradient concept has also been introduced to model nonlinear material behaviors. In the context of

* Corresponding authors.
E-mail addresses: raoyipeng@lsec.cc.ac.cn (Y. Rao), xiang_meizhen@iapcm.ac.cn (M. Xiang), cjz@lsec.cc.ac.cn (J. Cui).

https://doi.org/10.1016/j.jmps.2021.104752
Received 19 August 2021; Received in revised form 3 December 2021; Accepted 14 December 2021
Available online 4 January 2022

plasticity, strain gradient theory has gotten a booming development since the early 1980s. Representative contributions including the Aifantis theory (Aifantis, 1983), the Fleck–Hutchinson theory (Fleck and Hutchinson, 1993, 1997, 2001), the mechanism-based plasticity theory (Nix and Gao, 1998; Gao and Hutchinson, 1999; Han et al., 2004), the Gurtin theory (Gurtin, 2002), the Mentzel and Steinmann theory (Menzel, 2000) and the Gudmundson theory (Gudmundson, 2004) among others. In damage and fracture mechanics, the strain gradient elasticity or plasticity are used to investigate stress and strain fields around single crack tip (see for example Martínez-Pañeda and Fleck (2019), Chen et al. (1999), Goutianos (2011), Gei and Radi (2003), Jiang et al. (2001)). In addition, the strain gradients are also incorporated into fracture criterion or damage evolution equations in materials with many micro-cracks inside (Peerlings et al., 1996; Li, 2011; Li et al., 2011; Kuliev and Morozov, 2016; Nguyen and Niiranen, 2020).

Now, after the excellent capabilities of strain gradient theories for modeling scale-dependent phenomena are well confirmed, determining the high-order gradient modulus using "bottom-up" multiscale techniques become important and popular topics. For example, recent works (Xiang et al., 2012; Sunyk and Steinmann, 2003; Admal et al., 2017) have focused on deriving the elastic tensors of first strain-gradient elasticity based on atomistic potential and lattice structure using continuum–atomistic coupling approach. The basic idea of these works is to express strain energy in term of atomistic potential functions, where strain gradients enter into energy function through Taylor expansion at reference atomistic configuration. To involve nonlocal interactions of microstructures at mesoscales between the atomistic scale and the macroscale, homogenization of a Representative Volume Elements (RVE) including the gradient terms of the macroscopic field is widely used. Drugan and Willis (1996) and Drugan (2000) generalized the Hashin–Shtrikman variational formulation to derive micromechanics-based variational estimates for a higher-order nonlocal constitutive equation relating the ensemble averages of stress and strain, for a class of random linear elastic composite materials. Geers et al. (2001) and Kouznetsova et al. (2002) proposed a gradient-enhanced computational procedure that extends the classical computational homogenization technique to a full-gradient geometrically non-linear approach, leading to gradient-enhanced continuum model. In this method the macroscopic deformation and its gradient are used to prescribe the essential boundary conditions on a microstructural RVE. From the solution of the RVE boundary value problem, the macroscopic stress tensor and the higher-order stress tensor are extracted by enhanced Hillandel condition. Li (2011) developed strain gradient constitutive relations for heterogeneous materials based on construction of the average strain-energy density for a well-chosen RVE by using a self-consistent homogenization technique. By introducing a resistance curve into the strain-gradient constitutive law, Li et al. (2011) obtained an energy potential that is capable to describe the evolution of damage during the loading.

Apart from these mechanical homogenization procedures which use strain gradient as kinematic constraints on the RVE, another approach for deriving strain gradient laws is to use the multiscale asymptotic expansion method which has been well developed in the mathematical literature on periodic homogenization (Bensoussan et al., 1978; Oleinik et al., 1992). Triantafyllidis and Bardenhagen (1996) used the multiscale asymptotic technique to express the critical load at the onset of the first instability of periodic solids in terms of the scale parameter ε and higher order gradient macroscopic modulus. Smyshlyaev and Cherednichenko (2000) constructed higher order effective constitutive relations using the multiscale asymptotic technique on the basis of variational problems for the scalar problem of antiplane shear. Peerlings and Fleck (2004) extended this method to calculate strain gradient modulus in three-dimensional linear elasticity. In these multiscale asymptotic technique-based methods, the calculations of strain gradient modulus constants all require solving boundary value problems on the unit cell. Forest et al. (2001) developed asymptotic expansion analysis for periodic heterogeneous elastic Cosserat media, showing that the nature of the homogeneous equivalent medium depends on the hierarchy of three characteristic lengths: the size of the heterogeneities, the Cosserat intrinsic lengths of the constituents and the typical size of the considered structure.

In this work, we derive a strain gradient constitutive law for brittle materials with many micro-cracks inside. For this purpose, the two-scale asymptotic techniques (Cao and Cui, 1999; Ma et al., 2016; Dong et al., 2018) are used in combination with the Griffith fracture criterion. We noted that Dascalu et al. (2008) and Keita et al. (2014) have used two-scale asymptotic techniques to model brittle fracture. They expressed the energy release rate by two-scale approximate expansion to obtain a brittle fracture criterion and a damage evolution law in form of the macro effective elastic tensor as a function of the damage variable (crack length). The present work utilizes the two-scale approximate expansion technique in a quite different manner from that in Dascalu et al. (2008) and Keita et al. (2014). We approximate the strain energy, instead of energy release rate (as in Dascalu et al. (2008) and Keita et al. (2014)), by the two-scale approximate expansion solution. This novel strategy leads to a brittle fracture model that involves strain gradient terms, which are absent in models derived in Dascalu et al. (2008) and Keita et al. (2014). The resulted model allows us to conduct coupled-analysis of strain gradient effects and microstructure size effects on brittle fracture.

The work is organized as follows: The model problem is proposed in Section 2, where a two-scale framework involving homogenized equilibrium equations and unit cell problems are established. In Section 3, strain energy density and the corresponding energy release rate based on the two-scale asymptotic homogenization techniques is deduced; And a macro fracture criterion is obtained by combining the Griffith fracture criterion for micro-cracks. In Section 4, numerical simulations are presented to test and validate the model. Throughout this paper, the Einstein summation convention for repeated indices is adopted.

2. Modeling

2.1. Two-scale modeling framework

We model brittle materials through a two-scale framework: macro structures are modeled as homogenized continuum; mechanical responses of a macroscopic material point are described by a representative volume element (RVE) containing micro-cracks; the failure of a macro material point is attributed to extension of micro-cracks. In real materials, micro-cracks with various shapes and

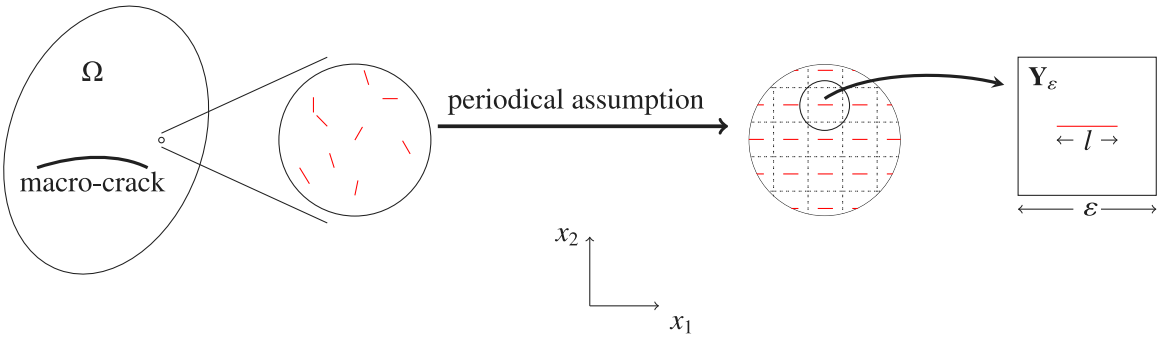

Fig. 1. Illustration of the two scale modeling framework and the local periodic assumption.

lengths are randomly distributed, as shown in the left part of Fig. 1. Here, as the first step, we simplify the structure of the cracked RVE by a local periodic assumption, as illustrated in Fig. 1. The unit cell of the periodic RVE contains a straight micro-crack with length l. The length (denoted as ε) of the unit cell physically represents mean distance between micro-cracks. We denote $d = l/\varepsilon$ which can be viewed as a variable that measures the damage extent; $d = 1$ indicates complete fracture. We further assume that ε is a fixed constant while micro-crack length d changes during loading.

The macro-scale governing equation is represented as:

$$\frac{\partial \Sigma_{ij}}{\partial X_j} = 0 \qquad \text{in} \quad \Omega \tag{1}$$

where $\{\Sigma_{ij}\}$ is the macro stress tensor and $\boldsymbol{X}$ is coordinates in the macro structure. Before failure, the stress–strain relation is

$$\Sigma_{ij} = C_{ijkl}\mathcal{E}_{kl} \tag{2}$$

where $\{C_{ijkl}\}$ is the homogenized elastic tensor which depends on microstructure and $\boldsymbol{\mathcal{E}}$ is the macro strain tensor that can be expressed as:

$$\mathcal{E}_{ij} = \frac{1}{2}\left(\frac{\partial U_i}{\partial X_j} + \frac{\partial U_j}{\partial X_j}\right) \tag{3}$$

where $\boldsymbol{U}$ is displacement field in the macro structure.

Provided that the constitutive model of the matrix material (excluding cracks) is known, closing the macro continuum model for brittle fracture requires answers for two issues. The first issue is to determine relation between macroscopic effective elastic tensor $\boldsymbol{C}$ and the microstructural variables ε, d, i.e., $\boldsymbol{C} = \boldsymbol{C}(\varepsilon, d)$. The second issue is to determine a failure criterion or evolution law of microstructural variables under loading. In following sections, we address these issues in a self-consistent manner using the asymptotic expansion techniques for heterogeneous materials.

2.2. Asymptotic analysis of the periodical RVE problem

We denote the infinite periodical RVE as $\mathcal{B}(= \mathbb{R}^2)$ and the domain occupied by micro-cracks as C. In the solid part of the RVE $\mathcal{B}_s = \mathcal{B}\backslash C$, the equilibrium equation is

$$\frac{\partial \sigma^\varepsilon_{ij}}{\partial x_j} = 0 \qquad \text{in} \quad \mathcal{B}_s, \tag{4}$$

and the linear elastic constitutive relation is

$$\sigma^\varepsilon_{ij} = a_{ijkl} e_{kl}(\mathbf{u}^\varepsilon) \tag{5}$$

where $\mathbf{u}^\varepsilon$, $\boldsymbol{\sigma}^\varepsilon$ and $e_{ij}(\mathbf{u}^\varepsilon)$ represent displacement, stress and strain fields in the RVE and

$$e_{ij}(\mathbf{u}^\varepsilon) = \frac{1}{2}\left(\frac{\partial u^\varepsilon_i}{\partial x_j} + \frac{\partial u^\varepsilon_j}{\partial x_i}\right). \tag{6}$$

We assume isotropic elasticity of the solid material in the RVE:

$$a_{ijkl} = \lambda\delta_{ij}\delta_{kl} + \mu(\delta_{ik}\delta_{jl} + \delta_{il}\delta_{jk}) \tag{7}$$

where λ and μ the Lamé constants; δ_{ij} is the *Kronecker symbol*.

In this work, we only consider possible extension of cracks and ignore crack closure. As a result, the boundary condition at crack surfaces is:

$$\boldsymbol{\sigma}^\varepsilon \cdot \mathbf{n} = 0; \quad \left[\mathbf{u}^\varepsilon \cdot \mathbf{n}\right] > 0 \tag{8}$$

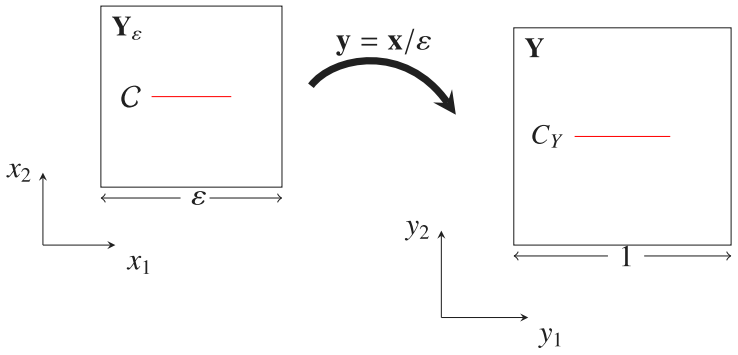

Fig. 2. Scale transformation.

where $\mathbf{n}$ is the outward unit normal vector on crack surfaces; $[\cdot]$ represents the jump across the crack faces.

With scale transformation $\mathbf{y} = \mathbf{x}/\varepsilon$, we can map the periodicity cell to a unit reference cell $Y = [0,1] \times [0,1]$ (see Fig. 2). Correspondingly, the crack C maps to C_Y with length $d = l/\varepsilon$ in Y; the upper and lower surface of the micro-crack in Y is marked as C_Y^+, C_Y^- respectively. The solid part in the reference cell is denoted as $Y_s = Y \backslash C_Y$. The introduction of the two-scale variables implies following chain rule of derivatives:

$$\frac{\mathrm{d}}{\mathrm{d}x_i} = \frac{\partial}{\partial x_i} + \frac{1}{\varepsilon}\frac{\partial}{\partial y_i}. \tag{9}$$

Based on the asymptotic homogenization method (Bensoussan et al., 1978), we can find an expansion of the RVE solution $\mathbf{u}^\epsilon$ in the following form:

$$\mathbf{u}^\epsilon(\mathbf{x}) = \mathbf{u}^{(0)}(\mathbf{x},\mathbf{y}) + \varepsilon\mathbf{u}^{(1)}(\mathbf{x},\mathbf{y}) + \varepsilon^2\mathbf{u}^{(2)}(\mathbf{x},\mathbf{y}) + \cdots \tag{10}$$

where $\mathbf{u}^{(i)}(\mathbf{x},\mathbf{y}), (i \in \mathbb{N})$ are Y-periodic about micro variable $\mathbf{y}$.

For simplicity, we introduce following notations for symmetric parts of spatial derivatives of a vector function $\mathbf{f}(\mathbf{x},\mathbf{y})$:

$$e_{xij}(\mathbf{f}) = \frac{1}{2}\left(\frac{\partial f_i}{\partial x_j} + \frac{\partial f_j}{\partial x_i}\right), \qquad e_{yij}(\mathbf{f}) = \frac{1}{2}\left(\frac{\partial f_i}{\partial y_j} + \frac{\partial f_j}{\partial y_i}\right).$$

And we define the following space:

$$\mathcal{D}(Y_s) = \left\{\mathbf{u}\middle|\mathbf{u} \in [H^1(Y_s)]^2,\ \mathbf{u} \text{ is } Y-\text{periodic in } y,\ \int_{Y_s}\mathbf{u}\,\mathrm{d}y = 0\right\}.$$

where $H^1(Y_s)$ denotes the Sobolev space (Cioranescu and Donato, 1999).

By substituting the asymptotic expansion Eq. (10) into Eq. (4) and comparing coefficients for terms with the same order of ε, we obtain a series of partial differential equations defined in the unit cell:

$$\begin{cases} \dfrac{\partial}{\partial y_j}\left(a_{ijkl}e_{ykl}(\mathbf{u}^{(0)})\right) = 0, & \text{in } Y_s, \\ a_{ijkl}e_{ykl}(\mathbf{u}^{(0)})n_j = 0, & \text{on } C_Y^\pm; \end{cases} \tag{11}$$

$$\begin{cases} \dfrac{\partial}{\partial y_j}\left(a_{ijkl}\left(e_{xkl}(\mathbf{u}^{(0)}) + e_{ykl}(\mathbf{u}^{(1)})\right)\right) = 0, & \text{in } Y_s, \\ a_{ijkl}\left(e_{ykl}(\mathbf{u}^{(1)}) + e_{xkl}(\mathbf{u}^{(0)})\right)n_j = 0, & \text{on } C_Y^\pm; \end{cases} \tag{12}$$

$$\begin{cases} \dfrac{\partial}{\partial x_j}a_{ijkl}\left(e_{xkl}(\mathbf{u}^{(0)}) + e_{ykl}(\mathbf{u}^{(1)})\right) + \dfrac{\partial}{\partial y_j}a_{ijkl}\left(e_{xkl}(\mathbf{u}^{(1)}) + e_{ykl}(\mathbf{u}^{(2)})\right) = 0, & \text{in } Y_s, \\ a_{ijkl}\left(e_{xkl}(\mathbf{u}^{(1)}) + e_{ykl}(\mathbf{u}^{(2)})\right)n_j = 0, & \text{on } C_Y^\pm. \end{cases} \tag{13}$$

It is known that $\mathbf{u}^{(0)}$ is independent of the microscopic variable $\mathbf{y}$, i.e., $\mathbf{u}^{(0)} = \mathbf{u}^{(0)}(\mathbf{x})$ (Bensoussan et al., 1978). And there is a solution $\mathbf{u}^{(1)} \in \mathcal{D}(Y_s)$ for Eq. (12) in the following form:

$$\mathbf{u}^{(1)}(\mathbf{x},\mathbf{y}) = \mathbf{N}^{pq}(\mathbf{y})e_{xpq}(\mathbf{u}^{(0)}(\mathbf{x})) \tag{14}$$

where $\mathbf{N}^{pq}(\mathbf{y}) \in \mathcal{D}(Y_s)$, $(p,q = 1,2)$ are the first-order cell solutions satisfying:

$$\begin{cases} \dfrac{\partial}{\partial y_j}\left(a_{ijkl}e_{ykl}\left(\mathbf{N}^{pq}\right) + a_{ijpq}\right) = 0, & \text{in } Y_s, \\ \left(a_{ijkl}e_{ykl}\left(\mathbf{N}^{pq}\right) + a_{ijpq}\right)n_j = 0, & \text{on } C_Y^\pm. \end{cases} \tag{15}$$

Due to the symmetry of a_{ijkl}, $\mathbf{N}^{pq}(\mathbf{y}) = \mathbf{N}^{qp}(\mathbf{y})$.

Eq. (13) can be integrated over Y_s to obtain the homogenized equilibrium equation:

$$\frac{\partial}{\partial x_j}\left(C_{ijkl}e_{xkl}(\mathbf{u}^{(0)})\right) = 0 \tag{16}$$

where

$$C_{ijkl} = \int_{Y_s} a_{ijkl} + a_{ijmn}e_{ymn}(\mathbf{N}^{kl})\ \mathrm{d}y \tag{17}$$

is the homogenized elastic tensor, which defines the effective elastic tensor at the macro continuum. Thus, Eq. (17) provides an answer for the first issue mentioned in Section 2. From Eq. (17) and noting that the integral is defined over solid part (Y_s) of the reference cell Y, C_{ijkl} depends only on d and is independent of ε.

3. Brittle fracture criterion based on asymptotic analysis

In this section, the fracture criterion is established by using the cell solutions defined above. Firstly, the local strain energy density E in the periodical RVE can be expressed as follows:

$$E = \frac{1}{2}\boldsymbol{\sigma}^{\varepsilon} : \boldsymbol{e}(\mathbf{u}^{\varepsilon}) = \frac{1}{2}a_{ijkl}e_{ij}(\mathbf{u}^{\varepsilon})e_{kl}(\mathbf{u}^{\varepsilon}). \tag{18}$$

Using the asymptotic expansion Eq. (10) and taking the first order $O(\varepsilon)$ approximation, we can obtain

$$e_{ij}(\mathbf{u}^{\epsilon})(\mathbf{x}) = e_{xij}(\mathbf{u}^0)(\mathbf{x}) + e_{yij}(\mathbf{N}^{pq})(\mathbf{y})e_{xpq}(\mathbf{u}^0)(\mathbf{x}) + \frac{\varepsilon}{2}\left(\mathbf{N}_i^{pq}(\mathbf{y})\frac{\partial e_{xpq}(\mathbf{u}^0)}{\partial x_j}(\mathbf{x}) + \mathbf{N}_j^{pq}(\mathbf{y})\frac{\partial e_{xpq}(\mathbf{u}^0)}{\partial x_i}(\mathbf{x})\right). \tag{19}$$

With the symmetry of a_{ijkl} and substituting Eq. (19) into Eq. (18), we obtain:

$$\begin{aligned} E = {} & \frac{1}{2}a_{ijkl}e_{xij}(\mathbf{u}^0)e_{xkl}(\mathbf{u}^0) + \frac{1}{2}a_{ijkl}\mathbf{N}_{i,j}^{pq}\mathbf{N}_{k,l}^{mn}e_{xpq}(\mathbf{u}^0)e_{xmn}(\mathbf{u}^0) + a_{ijkl}\mathbf{N}_{i,j}^{pq}e_{xpq}(\mathbf{u}^0)e_{xkl}(\mathbf{u}^0) \\ & + \varepsilon a_{ijkl}\left(e_{xij}(\mathbf{u}^0) + \mathbf{N}_{i,j}^{pq}e_{xpq}(\mathbf{u}^0)\right)\mathbf{N}_k^{mn}\frac{\partial e_{xmn}(\mathbf{u}^0)}{\partial x_l} + \frac{\varepsilon^2}{2}a_{ijkl}\mathbf{N}_i^{pq}\mathbf{N}_k^{mn}\frac{\partial e_{xpq}(\mathbf{u}^0)}{\partial x_j}\frac{\partial e_{xmn}(\mathbf{u}^0)}{\partial x_l}. \end{aligned} \tag{20}$$

Integrate Eq. (20) in Y_ε, we obtain the total strain energy of the unit cell:

$$W = \int_{Y_\varepsilon} E\mathrm{d}x.$$

Noting that $\boldsymbol{u}^0$ and its derivatives are slowly varying functions over the local domain Y_ε, we can approximate the strain energy W as:

$$\begin{aligned} W \approx {} & \langle e_{xpq}(\mathbf{u}^0)\rangle\langle e_{xmn}(\mathbf{u}^0)\rangle\int_{Y_\varepsilon}\frac{1}{2}a_{ijkl}\mathbf{N}_{i,j}^{pq}\left(\frac{\mathbf{x}}{\varepsilon}\right)\mathbf{N}_{k,l}^{mn}\left(\frac{\mathbf{x}}{\varepsilon}\right)\ \mathrm{d}x + \langle e_{xpq}(\mathbf{u}^0)\rangle\langle e_{xkl}(\mathbf{u}^0)\rangle\int_{Y_\varepsilon}a_{ijkl}\mathbf{N}_{i,j}^{pq}\left(\frac{\mathbf{x}}{\varepsilon}\right)\ \mathrm{d}x \\ & + \frac{\varepsilon^2}{2}a_{ijkl}\langle e_{xij}(\mathbf{u}^0)\rangle\langle e_{xkl}(\mathbf{u}^0)\rangle + \frac{\varepsilon^2}{2}\langle\frac{\partial e_{xpq}(\mathbf{u}^0)}{\partial x_j}\rangle\langle\frac{\partial e_{xmn}(\mathbf{u}^0)}{\partial x_l}\rangle\int_{Y_\varepsilon}a_{ijkl}\mathbf{N}_i^{pq}\left(\frac{\mathbf{x}}{\varepsilon}\right)\mathbf{N}_k^{mn}\left(\frac{\mathbf{x}}{\varepsilon}\right)\ \mathrm{d}x, \end{aligned} \tag{21}$$

where $\langle\cdot\rangle = \int_{Y_\varepsilon}\cdot\,\mathrm{d}x/|Y_\varepsilon|$ represents volume average over Y_ε. In Eq. (21), the term corresponding to ε is zero due to the symmetry and anti-symmetry properties of the first-order cell solutions (see detailed proof in Appendix B). Using the variable substitution $\mathbf{y} = \mathbf{x}/\varepsilon$, we obtain:

$$\begin{aligned} W = {} & \frac{\varepsilon^2}{2}a_{ijkl}\langle e_{xij}(\mathbf{u}^0)\rangle\langle e_{xkl}(\mathbf{u}^0)\rangle + \frac{\varepsilon^2}{2}\langle e_{xpq}(\mathbf{u}^0)\rangle\langle e_{xmn}(\mathbf{u}^0)\rangle\int_{Y_s}a_{ijkl}\mathbf{N}_{i,j}^{pq}(\mathbf{y})\mathbf{N}_{k,l}^{mn}(\mathbf{y})\ \mathrm{d}y \\ & + \varepsilon^2\ \langle e_{xpq}(\mathbf{u}^0)\rangle\langle e_{xkl}(\mathbf{u}^0)\rangle\int_{Y_s}a_{ijkl}\mathbf{N}_{i,j}^{pq}(\mathbf{y})\ \mathrm{d}y + \frac{\varepsilon^4}{2}\langle\frac{\partial e_{xpq}(\mathbf{u}^0)}{\partial x_j}\rangle\langle\frac{\partial e_{xmn}(\mathbf{u}^0)}{\partial x_l}\rangle\int_{Y_s}a_{ijkl}\mathbf{N}_i^{pq}(\mathbf{y})\mathbf{N}_k^{mn}(\mathbf{y})\ \mathrm{d}y \\ = {} & \frac{\varepsilon^2}{2}\langle e_{xpq}(\mathbf{u}^0)\rangle\langle e_{xkl}(\mathbf{u}^0)\rangle\int_{Y_s}\left(a_{pqkl} + a_{klij}\mathbf{N}_{i,j}^{pq}(\mathbf{y})\right)\ \mathrm{d}y \\ & + \frac{\varepsilon^2}{2}\langle e_{xpq}(\mathbf{u}^0)\rangle\langle e_{xmn}(\mathbf{u}^0)\rangle\int_{Y_s}\left(a_{klpq} + a_{klij}\mathbf{N}_{i,j}^{pq}(\mathbf{y})\right)\mathbf{N}_{k,l}^{mn}(\mathbf{y})\ \mathrm{d}y \\ & + \frac{\varepsilon^4}{2}\langle\frac{\partial e_{xpq}(\mathbf{u}^0)}{\partial x_j}\rangle\langle\frac{\partial e_{xmn}(\mathbf{u}^0)}{\partial x_l}\rangle\int_{Y_s}a_{ijkl}\mathbf{N}_i^{pq}(\mathbf{y})\mathbf{N}_k^{mn}(\mathbf{y})\ \mathrm{d}y \\ = {} & \frac{\varepsilon^2}{2}C_{pqkl}\langle e_{xpq}(\mathbf{u}^0)\rangle\langle e_{xkl}(\mathbf{u}^0)\rangle + \frac{\varepsilon^4}{2}D_{pqjmnl}\langle\frac{\partial e_{xpq}(\mathbf{u}^0)}{\partial x_j}\rangle\langle\frac{\partial e_{xmn}(\mathbf{u}^0)}{\partial x_l}\rangle \end{aligned} \tag{22}$$

where

$$D_{pqjmnl} = \int_{Y_s}a_{ijkl}\mathbf{N}_i^{pq}(\mathbf{y})\mathbf{N}_k^{mn}(\mathbf{y})\mathrm{d}y. \tag{23}$$

In deriving Eq. (22), the equality

$$\int_{Y_s}\left(a_{klpq}+a_{klij}\mathbf{N}^{pq}_{i,j}(\mathbf{y})\right)\mathbf{N}^{mn}_{k,l}(\mathbf{y})\,\mathrm{d}y=\int_{Y_s}\left(a_{klpq}+a_{klij}e_{yij}(\mathbf{N}^{pq})\right)e_{ykl}(\mathbf{N}^{mn})\,\mathrm{d}y=0$$

is adopted (see detailed proof of in Appendix A).

For the cell including a crack, according to the Griffith criterion, crack extends when the energy release rate G exceeds a material-specific critical value G_c:

$$G>G_c. \tag{24}$$

When $G<G_c$, the crack is stable. We assume that crack extends straightly along the original direction. Under quasi-static loading, the energy release rate G is calculated as (Gross and Seelig, 2018):

$$G=-\frac{\mathrm{d}W}{\mathrm{d}l}. \tag{25}$$

With the substitution $d=l/\varepsilon$, we have:

$$\frac{\mathrm{d}(\ \cdot\ )}{\mathrm{d}l}=\frac{1}{\varepsilon}\frac{\mathrm{d}(\ \cdot\ )}{\mathrm{d}d}. \tag{26}$$

Then, the energy release rate can be rewritten as follows:

$$G=-\frac{\varepsilon}{2}\frac{\mathrm{d}C_{ijkl}(d)}{\mathrm{d}d}\langle e_{xij}(\mathbf{u}^0)\rangle\langle e_{xkl}(\mathbf{u}^0)\rangle-\frac{\varepsilon^3}{2}\frac{\mathrm{d}D_{pqjmnl}(d)}{\mathrm{d}d}\langle\frac{\partial e_{xpq}(\mathbf{u}^0)}{\partial x_j}\rangle\langle\frac{\partial e_{xmn}(\mathbf{u}^0)}{\partial x_l}\rangle. \tag{27}$$

The volume average of strain and strain gradients over a periodic cell can be viewed as macroscopic counterparts, i.e.,

$$\mathcal{E}_{ij}=\langle e_{xij}(\mathbf{u}^0)\rangle,\quad \mathcal{E}_{ij,k}=\langle\frac{\partial e_{xij}(\mathbf{u}^0)}{\partial x_k}\rangle. \tag{28}$$

Taking Eq. (28) into Eq. (27), we obtain the energy release rate in form of macro strain and strain gradient as:

$$G=-\frac{\varepsilon}{2}\frac{\mathrm{d}C_{ijkl}(d)}{\mathrm{d}d}\mathcal{E}_{ij}\mathcal{E}_{kl}-\frac{\varepsilon^3}{2}\frac{\mathrm{d}D_{pqjmnl}(d)}{\mathrm{d}d}\mathcal{E}_{pq,j}\mathcal{E}_{mn,l}. \tag{29}$$

Finally, we obtain the fracture criterion involving the effects of microstructure(ε and d) and strain gradient effects as:

$$-\frac{\varepsilon}{2}\frac{\mathrm{d}C_{ijkl}(d)}{\mathrm{d}d}\mathcal{E}_{ij}\mathcal{E}_{kl}-\frac{\varepsilon^3}{2}\frac{\mathrm{d}D_{pqjmnl}(d)}{\mathrm{d}d}\mathcal{E}_{pq,j}\mathcal{E}_{mn,l}>G_c. \tag{30}$$

Note that, although in the derivation process, we have used second order expansion term $\mathbf{u}^{(2)}$ in Eqs. (10) and (13). However, the resulted final model is only related to solutions of the first order unit cell problems $\mathbf{N}^{pq}$, and is not related to the second order unit cell solutions. The coefficients of the obtained fracture criterion is expressed in form of derivatives of effective elastic tensors C_{ijkl} and D_{pqjmnl} with respect to the normalized damage variable (d). C_{ijkl} and D_{pqjmnl} are calculated based on $\mathbf{N}^{pq}$ according to Eqs. (17) and (23). Although the derivation process is somewhat complex, the final form of the fracture criterion Eq. (30) is rather concise involving a strain-related term and a strain gradient-related term. This form of fracture criterion is similar to the that obtained by conventional self-consistent homogenization scheme (Li, 2011; Li et al., 2011).

Provided that the actual micro-crack distribution (described by ε and d) is determined, the fracture criteria is independent of the choice of the RVE. See detailed proof in Appendix C.

We anticipate here that Dascalu et al. (2008) has used two-scale asymptotic techniques to model brittle fracture. They expressed the energy release rate by two-scale approximate expansion and obtained a brittle fracture criterion. We utilize the two-scale approximate expansion technique in a quite different manner from that in Dascalu et al. (2008). We approximate the strain energy density, instead of the energy release rate (as in Dascalu et al. (2008)), by the two-scale approximate expansion. The resulted model involves strain gradient effects, which are absent in Dascalu et al. (2008). If the strain gradient term in our model is ignored, the present fracture criterion Eq. (30) exactly reduces to that provided by Dascalu et al. (2008).

4. Numerical results

Coefficients of the fracture criterion Eq. (30) are expressed in form of derivatives of the fourth- and sixth-order effective elastic tensors with respect to d (the normalized micro-crack length), i.e., $\frac{\mathrm{d}C_{ijkl}(d)}{\mathrm{d}d}$ and $\frac{\mathrm{d}D_{pqjmnl}(d)}{\mathrm{d}d}$. Before conducting numerical analysis, we firstly calculate values of C_{ijkl} and D_{pqjmnl} at 199 uniformly distributed points in the interval $d\in(0,1)$. Then by cubic spline interpolation, continuum functions $C_{ijkl}(d), D_{pqjmnl}(d)$ as well as $\frac{\mathrm{d}C_{ijkl}(d)}{\mathrm{d}d}$, $\frac{\mathrm{d}D_{pqjmnl}(d)}{\mathrm{d}d}$ are established. In numerical simulations, macro material point is viewed as fractured if $G>G_c$.

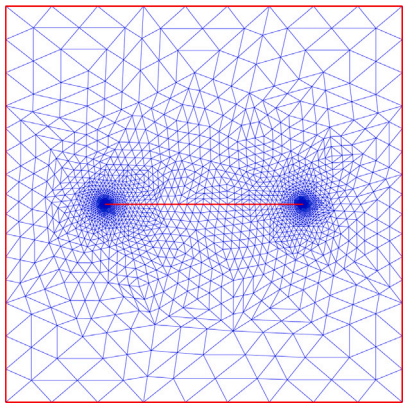

Fig. 3. The refined grids in the reference cell with $d = 0.5$.

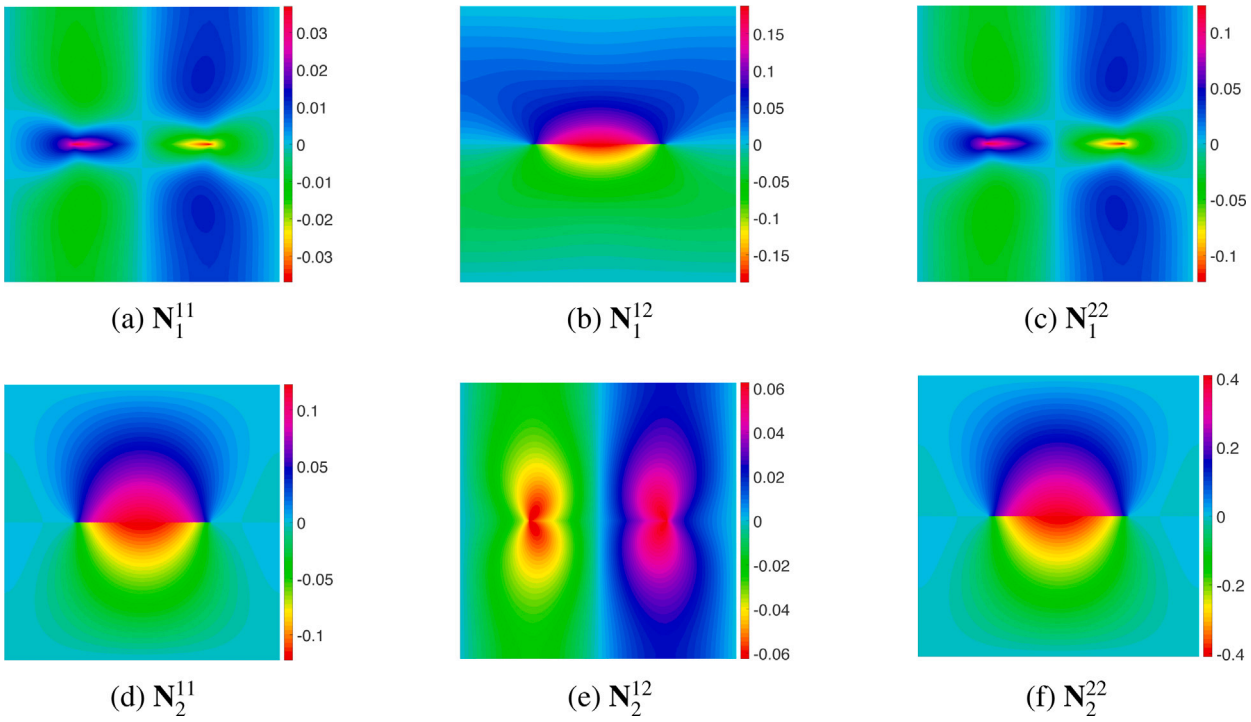

Fig. 4. First-order cell solutions $\mathbf{N}^{pq}(\mathbf{y})$ with damage $d = 0.5$.

4.1. Unit cell analysis

We consider brittle material with micro-cracks inside. The bulk solid (excluding cracks) is described by isotropic elasticity. In following discussions, unless otherwise stated, the defaulted constitutive constants are chosen as Young's modulus $E = 2$ GPa, Poisson ratio $\nu = 0.3$ and fracture energy $G_c = 1$ J/m^2.

First-order cell functions $\mathbf{N}^{pq}(\mathbf{y})$ are solved based on Eq. (15) using triangular meshes with refinement near crack tips, as displayed in Fig. 3. The numerical results for $\mathbf{N}^{pq}$ are displayed in Fig. 4. It is shown that the solutions are symmetric or anti-symmetric with respect to the axes which are parallel or perpendicular to the crack. Rigorous proof of symmetry or anti-symmetry of the cell solutions is provided in Appendix B.

Fig. 5(a) shows calculated components of the homogenized elastic tensor based on solutions of the first-order cell problems according to Eq. (17). The presence of micro-crack leads to anisotropy in the overall response. For materials with $d \to 0$, the homogenized coefficients are equal to initial modulus, that is $C_{1111}(0) = C_{2222}(0) = E/(1-\nu^2), C_{1122}(0) = C_{2211}(0) = E \times \nu/(1-\nu^2), C_{1212}(0) = E/(2 \times (1+\nu))$. Since $C_{1112} = C_{1222} \equiv 0$ due to the symmetry of $\mathbf{N}^{pq}(\mathbf{y})$, they are not shown in Fig. 5(a). It is shown that components C_{ijkl} decreases as d increases. As d increases, the elastic resistance along the direction vertical to the micro-crack

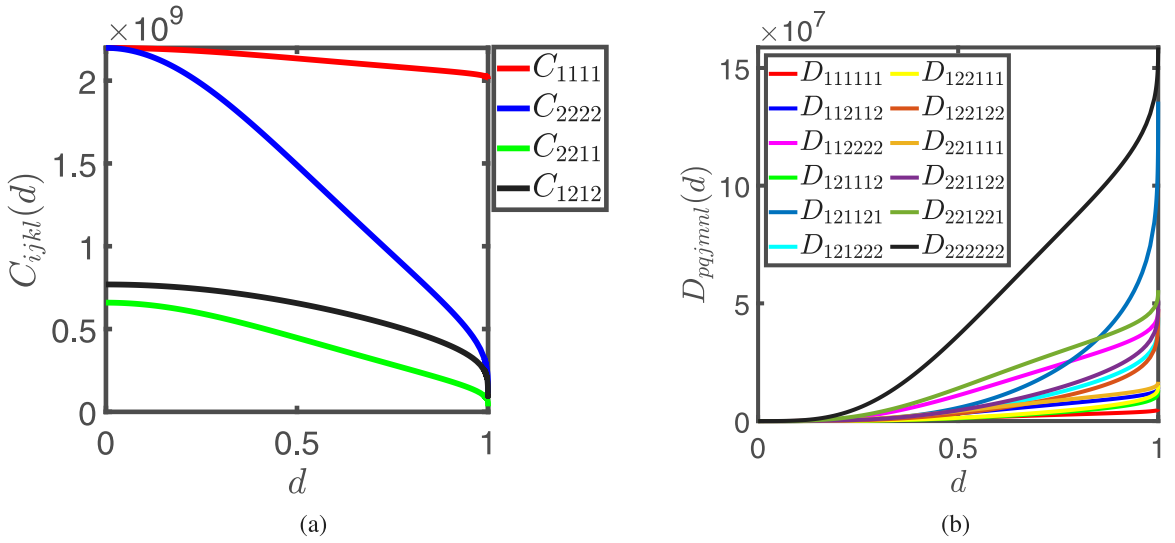

Fig. 5. (a)C_{ijkl} vs. d curve; (b)D_{pqjmnl} vs. d curve.

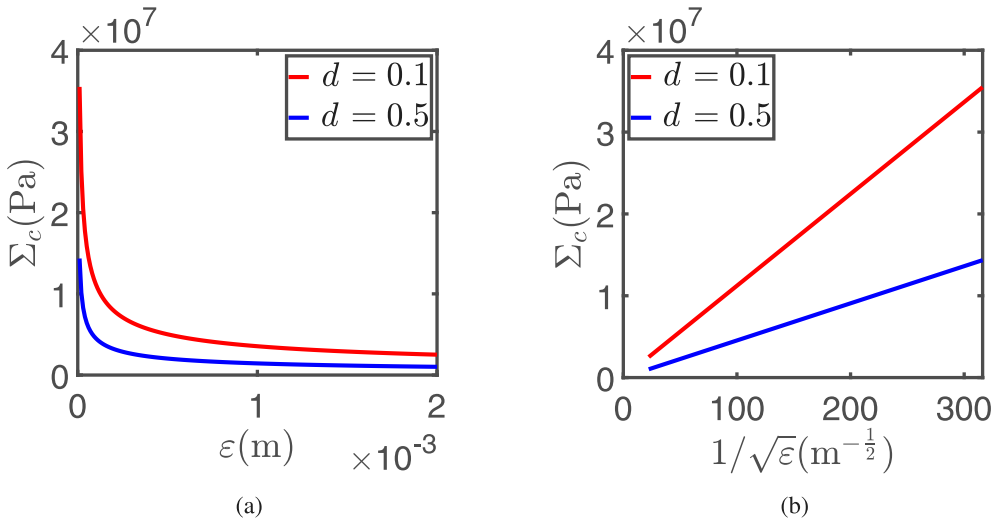

Fig. 6. Effects of ε on critical fracture stress, for $d = 0.1$ and $d = 0.5$.

(C_{2222}) decreases most remarkably, while the elastic resistance along the direction parallel to the micro-crack (C_{1111}) decreases most slowly.

Fig. 5(b) shows calculated components of the sixth-order tensor D_{pqjmnl} as a function of normalized crack length $d \in (0, 1)$. The symmetry of a_{ijkl} and $\mathbf{N}^{pq}$ leads to $D_{pqjmnl} = D_{qpjmnl} = D_{mnlpqj}$. According to the symmetry or anti-symmetry of the first-order cell solutions, the sixth-order tensor D_{pqjmnl} only has 12 non-zero components. Contrary to C_{ijkl}, D_{pqjmnl} all increase as d increases from 0 to 1. As a consequence, each component of $\frac{\mathrm{d}D_{pqjmnl}}{\mathrm{d}d} > 0$. According to Eq. (29), the energy release rate will reduce as strain gradient increases. Moreover, the energy release rate of the model that neglecting strain gradient effects would generally overestimate the energy release rate that involves strain gradient effects.

4.2. Local macroscopic material response

Firstly, we test the response of a macro material point under uniaxial tension with only one non-zero strain component $\mathcal{E}_{22}$ and only one non-zero strain gradient component $\mathcal{E}_{22,2}$.

As loading strain increases from zero, stress increases linearly until the fracture criterion $G = G_c$ fulfills. The stress at fracture is referred to as critical loading stress (or critical stress or fracture strength, denoted as Σ_c). Fig. 6 displays the critical stress Σ_c as a

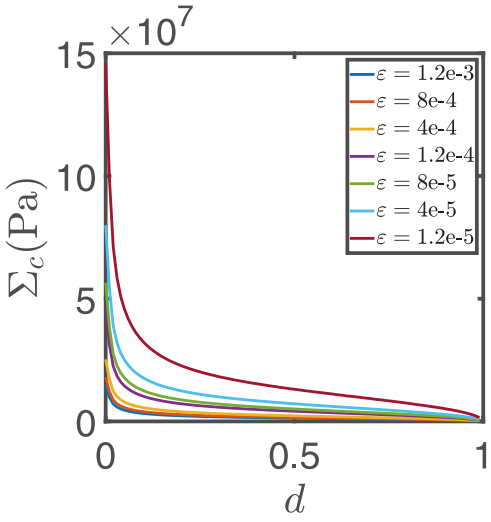

Fig. 7. Critical-stress as a function of d for different ϵ.

function of the microstructural size ϵ and $1/\sqrt{\epsilon}$ for fixed normalized micro-crack length d, when the strain gradient $\mathcal{E}_{22,2}$ is set to 0. From Fig. 6(a), it is shown that the critical fracture stress for $d = 0.1$ are always higher than that for $d = 0.5$ with different ϵ. The critical stress decreases as ϵ increases. Fig. 6(b) reveals a linear dependence of Σ_c on $1/\sqrt{\epsilon}$, indicating a Hall–Petch type size effect.

Fig. 7 displays the critical stress Σ_c as a function of the normalized micro-crack length d for different microstructural size ϵ, when the strain gradient $\mathcal{E}_{22,2}$ is set to 0. The critical stress decreases as d increases, representing softening effect of damage (micro-cracks). At the lower end of d (when $d < 0.1$), the critical stress decays very fast as d increases. When $d > 0.1$ the critical stress decline slowly to 0 as d approaches 1. This indicates that fracture strength of brittle material is more sensitive to the normalized micro-crack length d at the lower end (when $d < 0.1$).

Note that, in Fig. 7, Σ_c for $d = 0$ should be integrated as the limit fracture strength when the normalized micro-crack length approaches zero (from the positive side), i.e., $\Sigma_c(d = 0) = \lim_{d \to 0^+} \Sigma_c(d)$. Here, $d \to 0^+$ means that the length of micro-crack is negligible comparing to the mean distance between micro-cracks ($d \ll 1$, or $l \ll \epsilon$), or that there are defects (with negligible length) which serve as micro-crack nucleation sites. As indicated in Section 2, the parameter ϵ in the present two-scale framework has clear physical meaning — distance between micro-cracks or micro-crack nucleation sites. It is a material-dependent deterministic parameter and should not be chosen arbitrarily, even when $d \to 0^+$. Different ϵ represents different defect distribution. Therefore, Σ_c depends on ϵ even for the special case of $d \to 0^+$.

Fig. 8 displays the critical stress Σ_c as a function of strain gradient $\mathcal{E}_{22,2}$ for fixed microstructural size $\epsilon = 1 \times 10^{-3}$ m and damage variable $d = 0.5$. It is shown that the critical stress increases more and more fast as strain gradient increases. Fig. 9 displays the critical stress Σ_c as a function of the microstructural size ϵ under loading with different strain gradients. It is shown that the critical fracture stress is higher for larger strain gradient. Influence of strain gradient is negligible when ϵ is small ($\epsilon < 0.25 \times 10^{-3}$ m). As ϵ increases, influence of strain gradient becomes more significant. This result is consistent with previous knowledge, for example in Li et al. (2011).

4.3. Brittle fracture of macro structures

To study brittle fracture of macro structures, the macro continuum mechanics equations defined in Eqs. (1)–(3) are discretized by finite element methods. Macro structures are discretized by triangle meshes. To calculate the strain gradient effects, the Lagrangian P_2 element is used for displacement interpolation. And P_0 element is used for damage interpolation, which means damage is a constant in each triangle element. At each loading step and for each element, we calculate the strain and strain gradient at the centroid of the element. Then we check the energy release rate G defined by Eq. (29) using the pre-established function $\frac{\mathrm{d}C_{ijkl}(d)}{\mathrm{d}d}$, $\frac{\mathrm{d}D_{pqjmnl}(d)}{\mathrm{d}d}$. If $G > G_c$ then the element is viewed as fractured and the relevant mechanical parameters are updated instantly.

4.3.1. Mode-I crack extension

The first example is Mode-I crack extension, as illustrated in Fig. 10. A rectangular plate of dimension 0.1 m × 0.05 m, containing a V-notch with depth $b = 0.01$ m and span $a = 0.001$ m in the middle of the left side of the plate, is loaded by uniaxial tension. A unstructured triangular is generated using the Delaunay partition method with element length $h \approx 6.25 \times 10^{-4}$ m (the partition numbers along the rectangular boundaries are 100 and 200). The constitutive constants are chosen in consistence with that provided in Section 4.1. The plate is loaded in a quasi-static manner. At each loading step, a displacement increment $\Delta U = 5.00 \times 10^{-7}$ m is

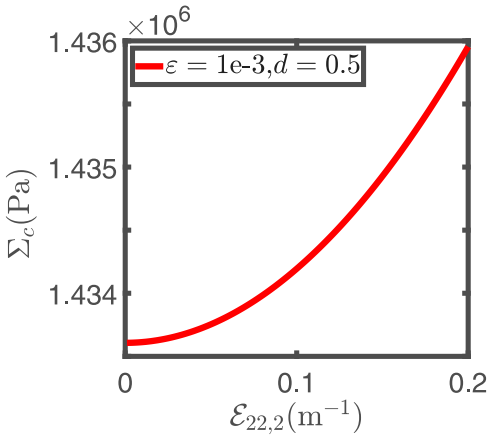

Fig. 8. Critical-stress and strain-gradient curve with $d = 0.5$ and $\varepsilon = 1\mathrm{e}-3\mathrm{m}$.

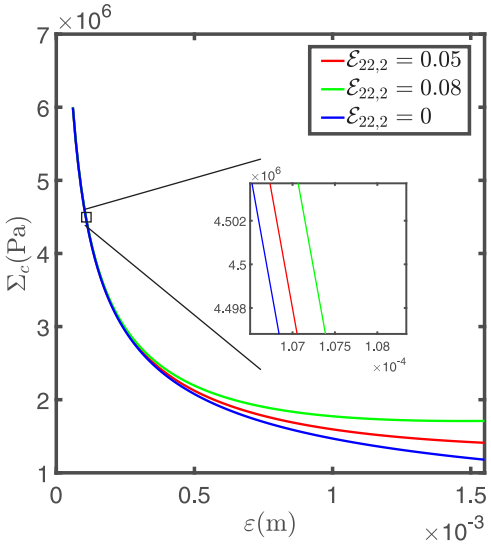

Fig. 9. Critical stress as a function of ε, for different strain gradient with damage $d = 0.5$.

Table 1
Critical loading stress (MPa) for different microstructure size (ε).

	$\varepsilon = 5\times10^{-4}$ m	$\varepsilon = 1\times10^{-3}$ m	$\varepsilon = 1.2\times10^{-3}$ m
Σ_c^{*}[a]	0.97	0.69	0.63
Σ_c[b]	0.99	0.74	0.82
Σ_c/Σ_c^{*}	1.02	1.07	1.30

[a] Σ_c^{*} represents calculated critical stress when the strain gradient term in Eq. (30) is neglected.
[b] Σ_c represents calculated critical stress strictly based on the fracture criterion Eq. (30) (involving the strain gradient term).

imposed on the bottom and up boundaries, as illustrated in Fig. 10. And iterations are conducted to obtain a converged solution at each loading step. Simulation stops when the macro crack run through the plate.

Table 1 illustrates the effects of microstructure size (ε) and strain gradient on the calculated critical loading stress. In simulations, the initial damage is set to $d = 0.1$. Σ_c represents calculated critical stress strictly based on the fracture criterion Eq. (30); Σ_c^{*} represents the calculated results when the strain gradient term in Eq. (30) is neglected. It is shown that Σ_c^{*} decreases as ε increases and $\Sigma_c^{*} < \Sigma_c$. These characteristics of microstructure size and strain gradient effects on fracture of macro-structure are consistent with the material response analysis in Section 4.2. From Table 1, Σ_c/Σ_c^{*} increases as ε increases, indicating that influences of strain gradient becomes more significant for larger microstructure size.

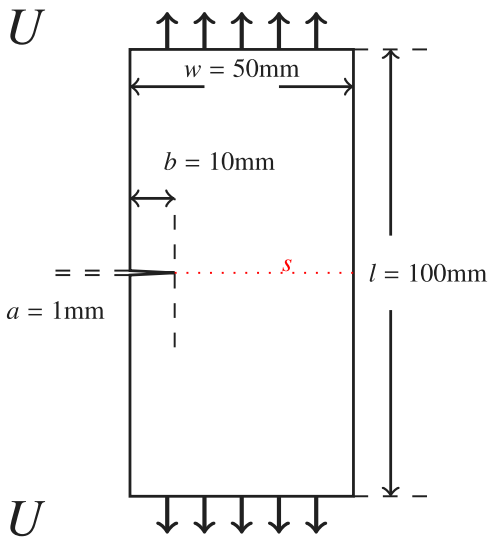

Fig. 10. Geometry of a V-notched plate.

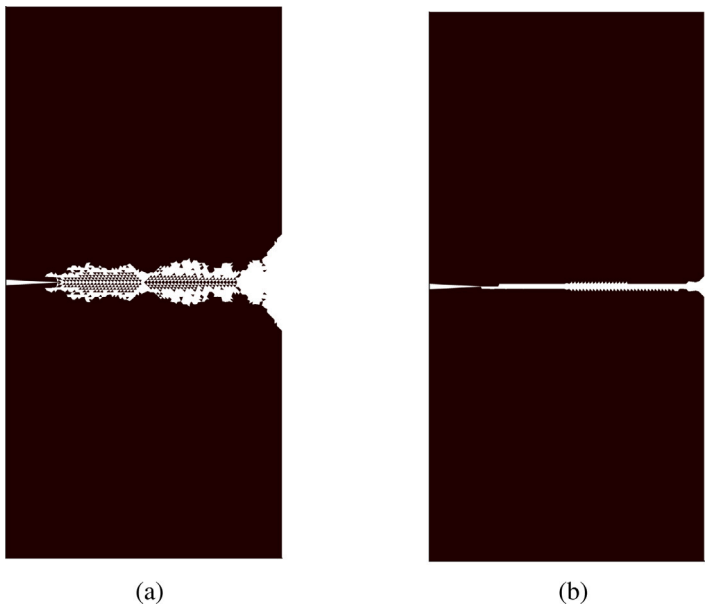

Fig. 11. Calculated fracture zones based on different fracture models: (a) with the strain gradient term; (b) without the strain gradient term.

Fig. 11 shows strain gradient effect on calculated fracture zone distribution when initial normalized micro-crack length is set to $d = 0.15$. Fig. 11(a) shows the calculated fracture zone strictly based on the fracture model Eq. (30); Fig. 11(b) shows the calculated fracture zone when the strain gradient term in Eq. (30) is neglected. It is shown that the present model Eq. (30) results in a wide fracture zone around the central line s. Neglecting the strain gradient term would lead to narrower fracture zone along the central line. Actually, involving strain gradient reduces stress concentration near the macro crack tip and leads to more homogeneous stress distribution around the macro crack. As a consequence, the calculated fracture zone with strain gradient effect is much more scattered than that without strain gradient effect.

4.3.2. Uniaxial tension of a holed plate

Secondly, we simulate uniaxial tension of a holed rectangular plate with dimensions $0.1\ \mathrm{m} \times 0.03\ \mathrm{m}$. A hole with radius r locates in the center of the plate, as shown in Fig. 12. The initial damage is set to $d = 0.1$. A Delaunay triangular mesh for the holed plate is denoted as $\mathcal{T}_h^{a,b,c}$, where a, b, c represent node counts on the horizontal, vertical and hole boundaries. In this numerical experiment,

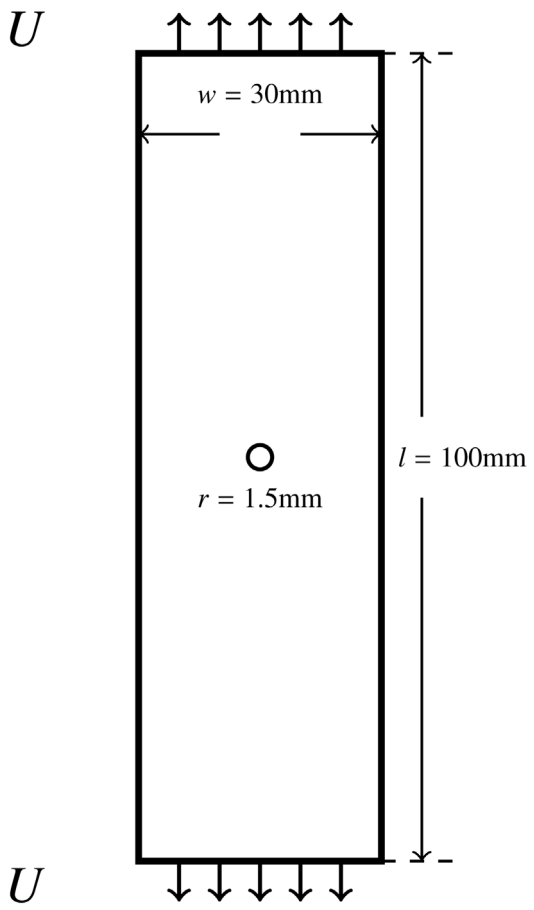

Fig. 12. Geometry for the holed plate.

the material parameters are chosen as Young's modulus $E = 3$ GPa, Poisson ratio $\nu = 0.36$ and fracture energy $G_c = 290$ J/m^2, in accordance with the experiments on PMMA (polymethylmethacrylate) provided in Li et al. (2011).

The displacement increment of each quasi-static loading step is set to $\Delta U = 1.00 \times 10^{-6}$ m. Fig. 13 displays the evolution of the fractured zone in a simulation with hole radius $r = 1.5 \times 10^{-3}$ m and $\varepsilon = 1 \times 10^{-3}$ m. At the loading step 516, two fracture zones start to initiate from the hole surface. As the fracture zones extend, the width of fracture zones increases. The final fracture zones show a curved triangle shape, as shown in Fig. 13(c).

It is widely known that involving strain gradient effects can reduce mesh-dependence of simulation results of fracture (Peerlings et al., 1996; Li, 2011; Li et al., 2011). To illustrate the mesh sensitivity of the present strain gradient model, we compare the calculated fracture zones using three different meshes $\mathcal{T}_h^{27,90,20}$, $\mathcal{T}_h^{36,120,24}$, $\mathcal{T}_h^{54,180,40}$ in Fig. 14. It is shown that shapes of the fracture zones obtained by the three different meshes are similar. The fracture zones obtained from the two finer meshes $\mathcal{T}_h^{36,120,24}$ and $\mathcal{T}_h^{54,180,40}$ have little difference, indicating a low mesh sensitivity of the calculated fracture zone when the mesh is fine enough.

Furthermore, the calculated critical loading stresses Σ_c (the maximum average stress at the loading boundary) using different meshes are listed in Table 2. For comparison purpose, the calculated critical loading stresses when the strain gradient term in Eq. (30) is neglected are also listed in Table 2 as Σ_c^*. It is shown that Σ_c^* has high mesh sensitivity. When strain gradient effect is neglected, refining the mesh leads to obviously reduction of Σ_c^*. However, the present model involving strain gradient effect results in a much lower mesh sensitivity of the critical load Σ_c, as shown in Table 2. Actually, the calculated Σ_c using the two meshes $\mathcal{T}_h^{36,120,24}$ and $\mathcal{T}_h^{54,180,40}$ have a subtle difference of 0.1 MPa (corresponding to a relative difference less than 0.4%). Consequently, we can confirm that involving the strain gradient effect greatly reduces mesh sensitivity of numerical results.

Numerical results in the rest part of this section are all obtained based on the mesh $\mathcal{T}_h^{54,180,40}$.

Table 3 displays the influences of ε on calculated critical stress Σ_c and Σ_c^*. Similar to the results in Table 1, it is shown that $\Sigma_c < \Sigma_c^*$ and Σ_c/Σ_c^* increases as ε increases, indicating that strain gradient effect becomes more significant for larger ε. It is in concordance with local macroscopic material responses as displayed in Fig. 8 in Section 4.2.

Fig. 15 shows the fracture zones of samples with different hole diameter. It is shown that the final fracture zone is larger for smaller hole radius.

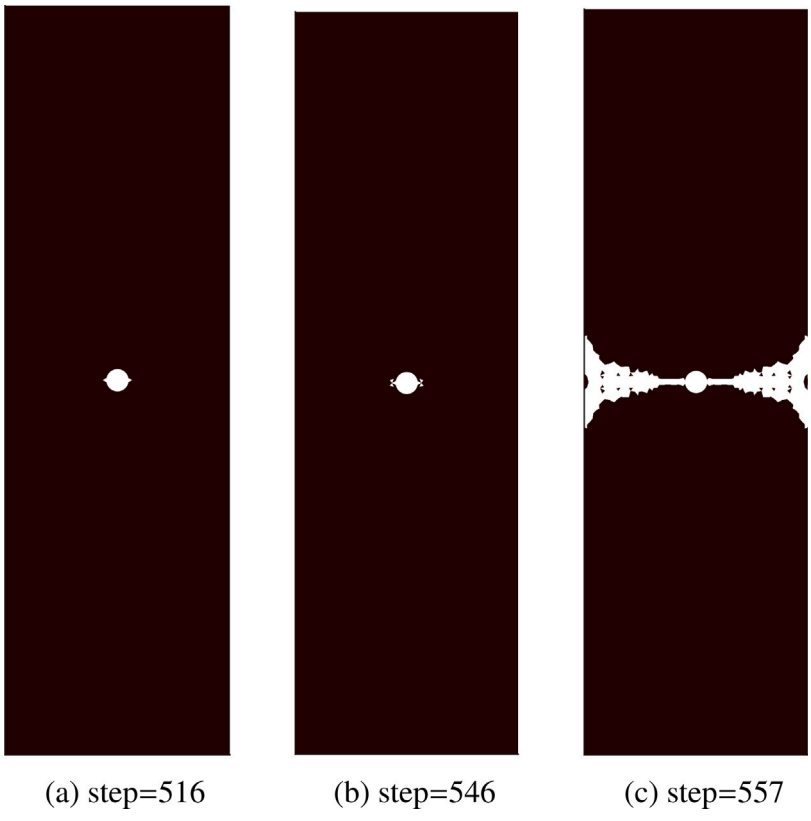

Fig. 13. Evolution of fracture zone in a holed plate with hole radius $r = 1.5 \times 10^{-3}$ m.

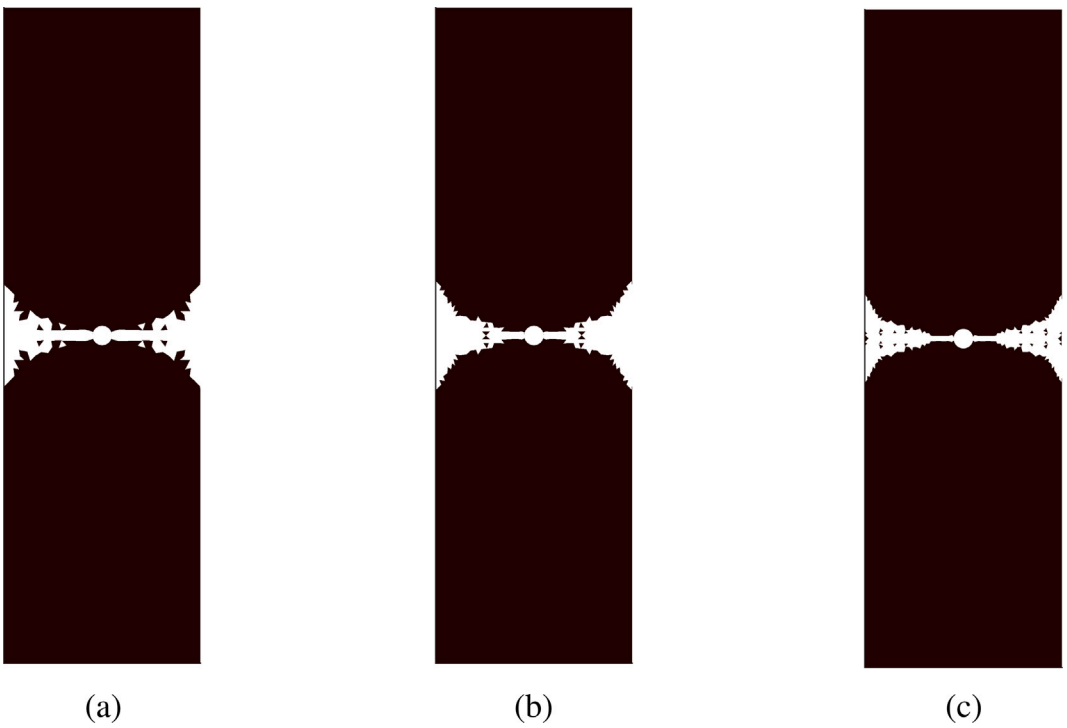

Fig. 14. Fracture zones for three different meshes: (a) $\mathcal{T}_h^{27,90,20}$; (b) $\mathcal{T}_h^{36,120,24}$; (c) $\mathcal{T}_h^{54,180,40}$.

Table 2
Calculated critical stress (MPa) based on different meshes[a].

	$\mathcal{T}_h^{27,90,20}$ (4976 elements)	$\mathcal{T}_h^{36,120,24}$ (9336 elements)	$\mathcal{T}_h^{54,180,40}$ (21248 elements)
Σ_c^*	18.7	17.0	14.7
Σ_c	27.1	26.0	25.9

[a]The results are obtained when $\epsilon = 4 \times 10^{-3}$ m, $r = 1.5 \times 10^{-3}$ m.

Table 3
Critical loading stress (MPa) for different ϵ[a].

	$\epsilon = 5 \times 10^{-4}$ m	$\epsilon = 1 \times 10^{-3}$ m	$\epsilon = 2 \times 10^{-3}$ m
Σ_c^*	48.6	34.6	24.1
Σ_c	49.3	35.7	34.9
Σ_c / Σ_c^*	1.01	1.03	1.44

[a]The results are obtained when $r = 1.5 \times 10^{-3}$ m.

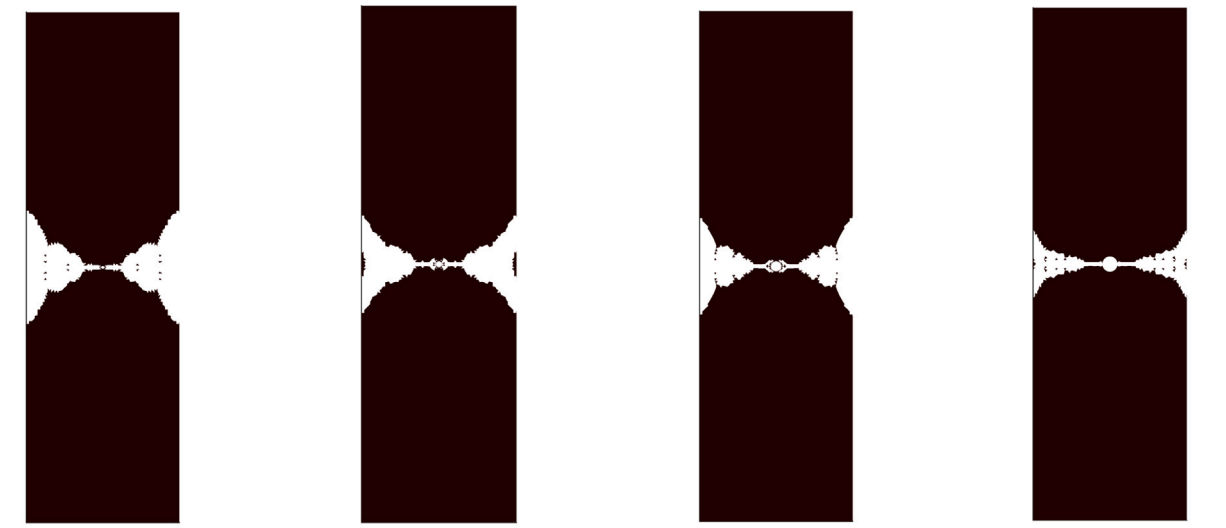

Fig. 15. Fracture zones in holed plates with different hole radius.

To further validate the present model, we compare calculated critical loading stresses with experimental data obtained by Li and Zhang (2006) in Fig. 16. Here, the microstructure parameter is calibrated to $\epsilon = 1 \times 10^{-3}$ m and initial damage is set to $d = 0.1$ and the critical stress for plate without hole is 72 MPa. The critical stress decreases as the hole diameter increases. The calculated critical stress using the strain gradient fracture criterion Σ_c are in good agreements with experimental data for the hole diameter varies from 0 to 3 mm. Neglecting the strain gradient term would leads to serious underestimation of the fracture strength (see Σ_c^* in Fig. 16).

5. Conclusion

In this paper, we have established a macro brittle fracture model for materials with many micro-cracks inside. The model is rigorously deduced based on a two-scale asymptotic analysis procedure, in combination of local periodical assumption of micro-crack distribution and the Griffith criterion for micro-crack extension. Strain gradient effects and microstructure size effects are naturally involved in the fracture criterion. Although the derivation process is complex, the resulted fracture criterion is concise. The model parameters are expressed in form of derivatives of the fourth- and sixth-order effective elastic tensors with respect to normalized micro-crack length. The elastic tensors are calculated through sub-scale solutions of first-order unit cell problems.

Numerical simulations indicate inspiring predictive abilities of the model. The model results in a Hall–Petch type microstructure size effects on fracture strength. The model predicts that the strength of brittle material is more sensitive to normalized micro-crack length d at the lower end. For small microstructure size ϵ, strain gradient effects is not obvious. As ϵ increases, strain gradient effects becomes more significant. Involving strain gradient effects leads to lower local energy release rate. Therefore, simulations based on the strain gradient fracture model result in higher fracture strength and wider fracture zone, comparing to simulations that neglect strain gradient effects. Based on the strain gradient fracture model, the calculated critical fracture stresses of holed PMMA plates are in well agreement with previous experimental data. Neglecting strain gradient leads to underestimation of the critical stress.

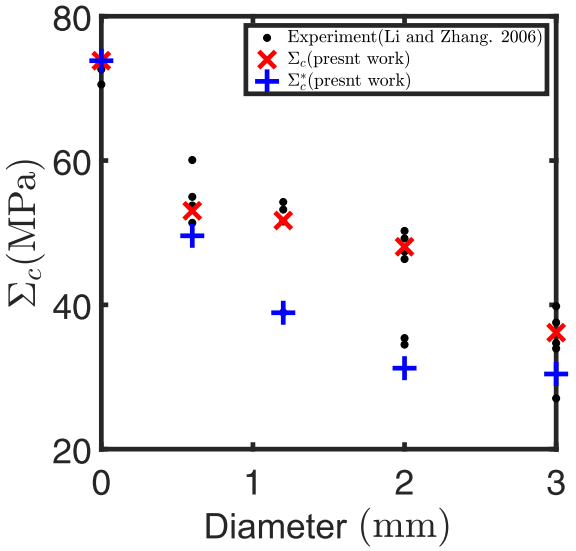

Fig. 16. Comparison between predicted critical loading stresses and experimental data for holed plates with different hole diameters; $\epsilon = 1 \times 10^{-3}$ m.

There are several limitations of the present work. Firstly, micro-inertia effects on dynamic micro-crack extension is not considered. As a consequence, the resulted macro model is a transient fracture criterion that cannot calculate the dynamic damage evolution processes. It can only apply to situations with quasi-static macro loading. For high strain rate problems, the dynamics of micro-crack extension must be taken into account. Secondly, closure of crack under compression state is not considered. These topics are left for future efforts.

CRediT authorship contribution statement

Yipeng Rao: Coding, Writing, Mathematical derivation. **Meizhen Xiang:** Conceptualization, Methodology, Validation, Supervision. **Junzhi Cui:** Supervision, Validation.

Declaration of competing interest

The authors declare that they have no known competing financial interests or personal relationships that could have appeared to influence the work reported in this paper.

Acknowledgment

The work is supported by the National Natural Science Foundation of China (No. 11772068, No.51739007), Strategic Priority Research Program of the Chinese Academy of Sciences (No.XDC06030101).

Appendix A. Symmetry of the homogenized coefficients C_{ijkl}

We prove $C_{pqkl} = C_{klpq}$.
The variational form of (15) is

$$\int_{Y_s} a_{ijpq} e_{yij}(\mathbf{v}) + a_{ijmn} e_{ymn}(\mathbf{N}^{pq}) e_{yij}(\mathbf{v}) \mathrm{d}y = 0, \forall \mathbf{v} \in \mathcal{D}(Y_s). \tag{A.1}$$

Taking $\mathbf{v} = \mathbf{N}^{kl}$, we obtain:

$$\int_{Y_s} a_{ijpq} e_{yij}(\mathbf{N}^{kl}) + a_{ijmn} e_{ymn}(\mathbf{N}^{pq}) e_{yij}(\mathbf{N}^{kl}) \mathrm{d}y = 0, \tag{A.2}$$

From the definition of C_{pqkl} in (17):

$$C_{pqkl} = \int_{Y_s} a_{pqkl} + a_{pqij} e_{yij}(\mathbf{N}^{kl}) \mathrm{d}y = \int_{Y_s} a_{pqkl} - a_{ijmn} e_{ymn}(\mathbf{N}^{pq}) e_{yij}(\mathbf{N}^{kl}) \mathrm{d}y, \tag{A.3}$$

It is clear that $C_{pqkl} = C_{klpq}$ due to $a_{ijmn} = a_{mnij}$.

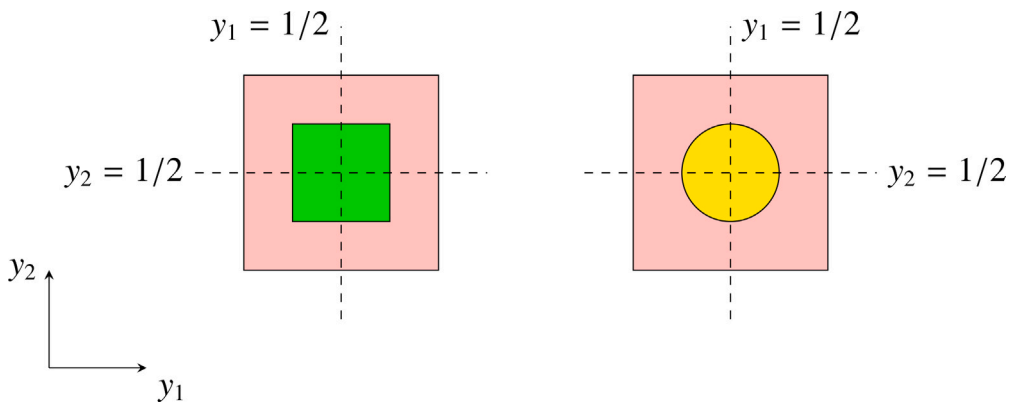

Fig. B.1. Two examples for cell configuration with symmetry to the middle plane $y_i = 1/2,\ i = 1, 2$.

Appendix B. Symmetry and anti-symmetry of first-order cell solutions

We show the symmetry and anti-symmetry of the first-order cell solutions for cell configuration which is symmetric about the line $y_i = 1/2\,(i = 1, 2)$, as sketched in Fig. B.1. Firstly, we consider $\mathbf{N}^{11}(y_1, y_2)$. We define a vector valued function $\bar{\mathbf{N}}^{11}(y_1, y_2)$ as

$$\bar{\mathbf{N}}_1^{11}(y_1, y_2) = -\mathbf{N}_1^{11}(1 - y_1, y_2), \qquad \bar{\mathbf{N}}_2^{11}(y_1, y_2) = \mathbf{N}_2^{11}(1 - y_1, y_2).$$

For a given test function $\mathbf{v}(y_1, y_2)$, we define:

$$\bar{\mathbf{v}}_1^{11}(y_1, y_2) = -\mathbf{v}_1^{11}(1 - y_1, y_2), \qquad \bar{\mathbf{v}}_2^{11}(y_1, y_2) = \mathbf{v}_2^{11}(1 - y_1, y_2).$$

From Eq. (A.1), we obtain:

$$\int_{Y_s} a_{ij11} e_{yij}(\bar{\mathbf{v}}) + a_{ijmn} e_{ymn}(\bar{\mathbf{N}}^{11}) e_{yij}(\bar{\mathbf{v}}) \mathrm{d}y = 0. \tag{B.1}$$

Comparing Eq. (B.1) and the special case of $\{p, q\} = \{1, 1\}$ in Eq. (A.1), we find that $\bar{\mathbf{N}}^{11}$ and $\mathbf{N}^{11}$ satisfies the same variational form. Thus, $\mathbf{N}_1^{11}(y_1, y_2) = \bar{\mathbf{N}}_1^{11}(y_1, y_2) = -\mathbf{N}_1^{11}(1 - y_1, y_2)$ and $\mathbf{N}_2^{11}(y_1, y_2) = \bar{\mathbf{N}}_2^{11}(y_1, y_2) = \mathbf{N}_2^{11}(y_1, 1 - y_2)$. Using similar analysis procedures, we obtain:

$$\begin{aligned}
&\mathbf{N}_1^{11}(y_1, y_2) = -\mathbf{N}_1^{11}(1 - y_1, y_2) = \mathbf{N}_1^{11}(y_1, 1 - y_2)\\
&\mathbf{N}_2^{11}(y_1, y_2) = -\mathbf{N}_2^{11}(y_1, 1 - y_2) = \mathbf{N}_2^{11}(1 - y_1, y_2)\\
&\mathbf{N}_1^{12}(y_1, y_2) = -\mathbf{N}_1^{12}(y_1, 1 - y_2) = \mathbf{N}_1^{12}(1 - y_1, y_2)\\
&\mathbf{N}_2^{12}(y_1, y_2) = -\mathbf{N}_2^{12}(1 - y_1, y_2) = \mathbf{N}_2^{12}(y_1, 1 - y_2)\\
&\mathbf{N}_1^{22}(y_1, y_2) = -\mathbf{N}_1^{22}(1 - y_1, y_2) = \mathbf{N}_1^{22}(y_1, 1 - y_2)\\
&\mathbf{N}_2^{22}(y_1, y_2) = -\mathbf{N}_2^{22}(y_1, 1 - y_2) = \mathbf{N}_2^{22}(1 - y_1, y_2).
\end{aligned} \tag{B.2}$$

Appendix C. RVE-independence of the fracture criterion

We illustrate that the fracture criterion Eq. (30) is independent of the choice of the size of the periodic RVE if the actual micro-crack distribution (described by ϵ and d) is determined.

We consider RVE sizes $k\epsilon \times k\epsilon$ where $k > 1$ is an integer .

Firstly, we consider $k = 2$. The RVE is a square with side length 2ϵ. Under the scale transformation $\mathbf{z} = \mathbf{x}/(2\epsilon)$, the RVE is mapped to the unit reference cell Z with side length 1, as illustrated in Fig. C.1. Z contains four micro-cracks, which is different from Y defined in Section 2 that contains only one micro-crack. The cracks in Z are indicated by C_Z and the solids part is denoted by $Z_s = Z \backslash C_Z$ as shown in Fig. C.1. Using microscale variable $\mathbf{z}$, the two-scale asymptotic expansion can be rewritten as:

$$\tilde{\mathbf{u}}^{2\epsilon}(\mathbf{x}) = \tilde{\mathbf{u}}^{(0)}(\mathbf{x}) + 2\epsilon \tilde{\mathbf{u}}^{(1)}(\mathbf{x}, \mathbf{z}) + 4\epsilon^2 \tilde{\mathbf{u}}^{(2)}(\mathbf{x}, \mathbf{z}) + \cdots \tag{C.1}$$

where $\tilde{\mathbf{u}}^{(i)}(\mathbf{x}, \mathbf{z}), (i \in \mathbb{N})$ are Z-periodic about micro variable $\mathbf{z}$.

Similar to Eq. (14), $\tilde{\mathbf{u}}^{(1)}(\mathbf{x}, \mathbf{z})$ can be written as follows:

$$\tilde{\mathbf{u}}^{(1)}(\mathbf{x}, \mathbf{z}) = \tilde{\mathbf{N}}^{pq}(\mathbf{z}) e_{xpq}(\tilde{\mathbf{u}}^{(0)}(\mathbf{x})) \tag{C.2}$$

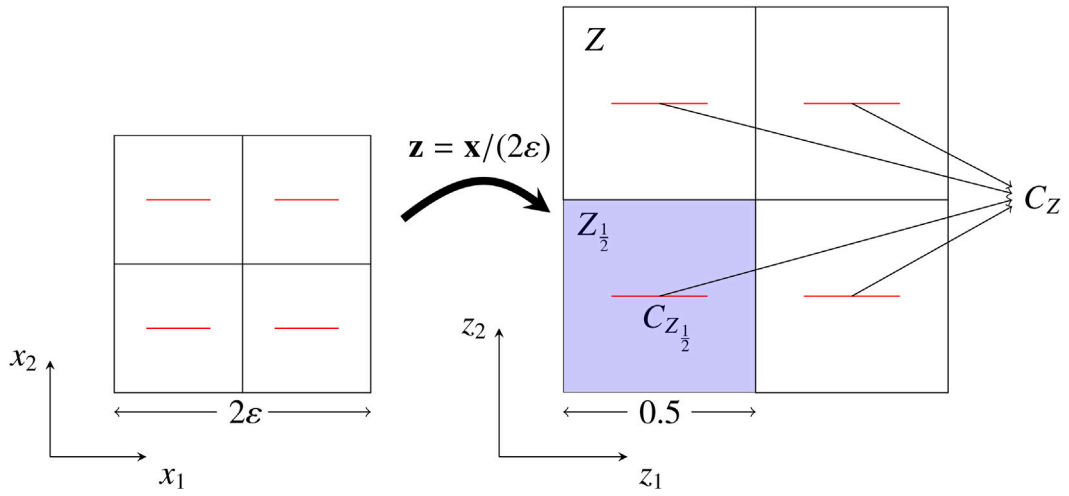

Fig. C.1. A cell configuration with size $2\varepsilon \times 2\varepsilon$ and the scale transformation.

where $\tilde{\mathbf{N}}^{pq}(\mathbf{z})$ is Z-periodic. It satisfies the following equation:

$$\begin{cases} \dfrac{\partial}{\partial z_j}\left(a_{ijkl}e_{zkl}\left(\tilde{\mathbf{N}}^{pq}\right) + a_{ijpq}\right) = 0, & \text{in } Z_s, \\ \left(a_{ijkl}e_{zkl}\left(\tilde{\mathbf{N}}^{pq}\right) + a_{ijpq}\right) n_j = 0, & \text{on } C_Z^{\pm}. \end{cases} \tag{C.3}$$

We use $Z_{\frac{1}{2}}$ to represent a sub-cell of Z that contains only one micro-crack, as indicated by the shaded part in Fig. C.1. The side length of $Z_{\frac{1}{2}}$ is 0.5. The solid part in $Z_{\frac{1}{2}}$ is $Z_{\frac{1}{2}s} = Z_{\frac{1}{2}} \backslash C_{Z_{\frac{1}{2}}}$. We define a $Z_{\frac{1}{2}}$-periodic function $\hat{\mathbf{N}}^{pq}(\mathbf{z})$ that satisfies the following equation:

$$\begin{cases} \dfrac{\partial}{\partial z_j}\left(a_{ijkl}e_{zkl}\left(\hat{\mathbf{N}}^{pq}\right) + a_{ijpq}\right) = 0, & \text{in } Z_{\frac{1}{2}s}, \\ \left(a_{ijkl}e_{zkl}\left(\hat{\mathbf{N}}^{pq}\right) + a_{ijpq}\right) n_j = 0, & \text{on } C_{Z_{\frac{1}{2}}}^{\pm}. \end{cases} \tag{C.4}$$

Note that $Z_{\frac{1}{2}s}$ and Y_s (defined in Section 2) has the following relation: $Y_s = \{2\mathbf{z} : \mathbf{z} \in Z_{\frac{1}{2}s}\}$. We define a function on Y_s by $\check{\mathbf{N}}^{pq}(\mathbf{z}) = \hat{\mathbf{N}}^{pq}(\mathbf{z}/2), \forall \mathbf{z} \in Y_s$. We can obtain that $e_{zkl}(\hat{\mathbf{N}}^{pq})\Big|_{\mathbf{z}/2} = 2e_{zkl}(\check{\mathbf{N}}^{pq})\Big|_{\mathbf{z}}$ and that $\check{\mathbf{N}}^{pq}(\mathbf{z})$ is Y-periodic. According to Eq. (C.4), $\check{\mathbf{N}}^{pq}$ satisfies:

$$\begin{cases} \dfrac{\partial}{\partial z_j}\left(a_{ijkl}e_{zkl}(2\check{\mathbf{N}}^{pq}) + a_{ijpq}\right) = 0, & \text{in } Y_s, \\ \left(a_{ijkl}e_{zkl}(2\check{\mathbf{N}}^{pq}) + a_{ijpq}\right) n_j = 0, & \text{on } C_Y^{\pm}. \end{cases} \tag{C.5}$$

Comparing Eq. (C.5) with Eq. (15), we find that $\check{\mathbf{N}}^{pq}(\mathbf{z}) = \mathbf{N}^{pq}(\mathbf{z})/2$, $\forall \mathbf{z} \in Y_s$; Equivalently $\hat{\mathbf{N}}^{pq}(\mathbf{z}) = \mathbf{N}^{pq}(2\mathbf{z})/2$, $\forall \mathbf{z} \in Z_{\frac{1}{2}s}$.

As $\hat{\mathbf{N}}^{pq}(\mathbf{z})$ is $Z_{\frac{1}{2}}$-periodic, we can periodically extend $\hat{\mathbf{N}}^{pq}(\mathbf{z})$ from $Z_{\frac{1}{2}s}$ to Z_s. Without introducing any confusions, the extended function defined on Z_s is still denoted as $\hat{\mathbf{N}}^{pq}(\mathbf{z})$. We find that $\hat{\mathbf{N}}^{pq}(\mathbf{z})$ satisfies the weak form of Eq. (C.3). According to Proposition 3.50 in Cioranescu and Donato (1999), we know that $\hat{\mathbf{N}}^{pq}(\mathbf{z}) \in [H^1(Z_s)]^2$. Then, according to the existence and uniqueness of weak solution of Eq. (C.3) in $[H^1(Z_s)]^2$, we obtain

$$\tilde{\mathbf{N}}^{pq}(\mathbf{z}) = \mathbf{N}^{pq}(2\mathbf{z})/2 \quad \text{a.e. on } Z_s. \tag{C.6}$$

This result can also be verified by comparing the calculated numerical results in Fig. C.2 with that in Fig. 4.

The first order $O(\varepsilon)$ approximation to $\tilde{\mathbf{u}}^{2\varepsilon}(\mathbf{x})$ is:

$$\begin{aligned} \tilde{\mathbf{u}}^{2\varepsilon}(\mathbf{x}) &= \tilde{\mathbf{u}}^{(0)}(\mathbf{x}) + 2\varepsilon\tilde{\mathbf{u}}^{(1)}(\mathbf{x}, \mathbf{z}) \\ &= \tilde{\mathbf{u}}^{(0)}(\mathbf{x}) + 2\varepsilon\tilde{\mathbf{N}}^{pq}(\mathbf{z})e_{xpq}(\tilde{\mathbf{u}}^{(0)}(\mathbf{x})) \\ &= \tilde{\mathbf{u}}^{(0)}(\mathbf{x}) + 2\varepsilon \cdot \frac{1}{2}\mathbf{N}^{pq}(2\mathbf{z})e_{xpq}(\tilde{\mathbf{u}}^{(0)}(\mathbf{x})) \\ &\overset{\mathbf{y}=2\mathbf{z}}{=\!=} \tilde{\mathbf{u}}^{(0)}(\mathbf{x}) + \varepsilon\mathbf{N}^{pq}(\mathbf{y})e_{xpq}(\tilde{\mathbf{u}}^{(0)}(\mathbf{x})). \end{aligned} \tag{C.7}$$

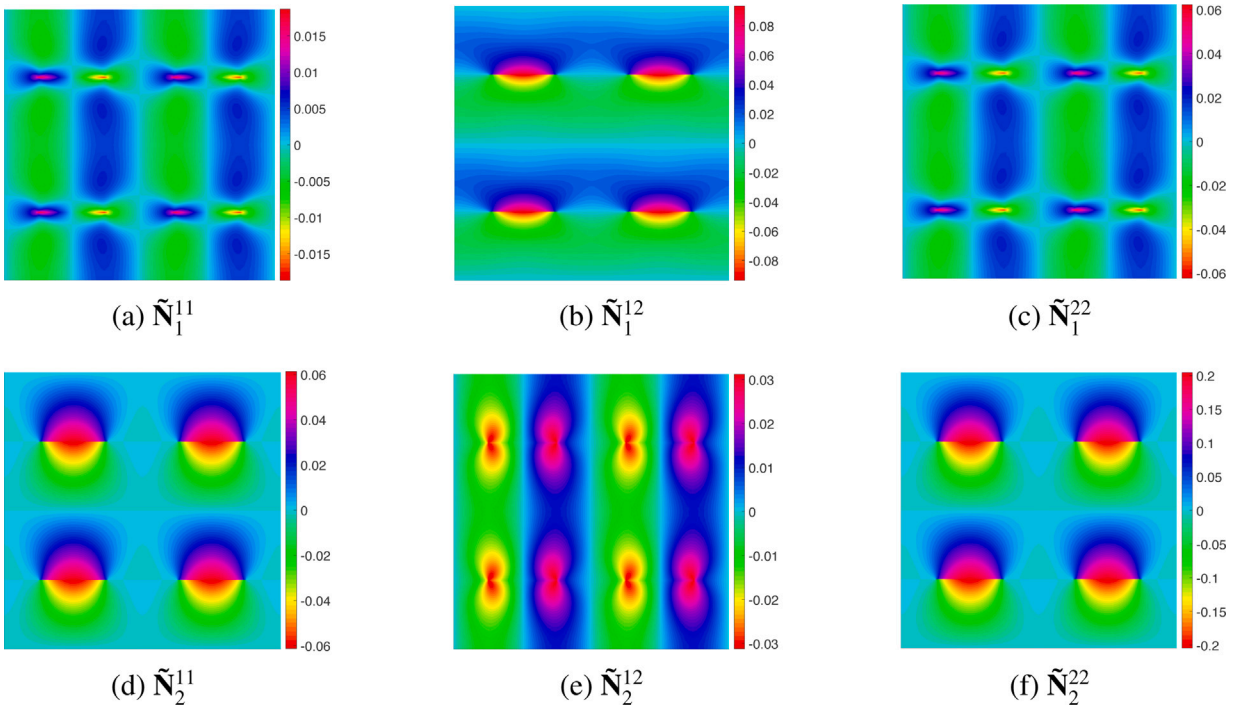

Fig. C.2. First-order unit cell solutions with four micro-cracks in the RVE.

Then we consider the following equation similar to Eq. (13):

$$\begin{cases} \dfrac{\partial}{\partial x_j} a_{ijkl}\left(e_{xkl}(\tilde{\mathbf{u}}^{(0)}) + e_{zkl}(\tilde{\mathbf{u}}^{(1)})\right) + \dfrac{\partial}{\partial z_j} a_{ijkl}\left(e_{xkl}(\tilde{\mathbf{u}}^{(1)}) + e_{zkl}(\tilde{\mathbf{u}}^{(2)})\right) = 0, & \text{in } Z_s, \\ a_{ijkl}\left(e_{xkl}(\tilde{\mathbf{u}}^{(1)}) + e_{zkl}(\tilde{\mathbf{u}}^{(2)})\right) n_j = 0, & \text{on } C_Z^{\pm}. \end{cases} \tag{C.8}$$

Integrate Eq. (C.8) over Z_s to obtain the homogenized equilibrium equation:

$$\frac{\partial}{\partial x_j}\left(\tilde{C}_{ijkl} e_{xkl}(\tilde{\mathbf{u}}^{(0)})\right) = 0 \tag{C.9}$$

where

$$\begin{aligned} \tilde{C}_{ijkl} &= \int_{Z_s} a_{ijkl} + a_{ijmn} e_{zmn}(\tilde{\mathbf{N}}^{kl})\Big|_{\mathbf{z}} \, \mathrm{d}z \\ &= 4 \int_{Z_{\frac{1}{2}s}} a_{ijkl} + a_{ijmn} e_{zmn}(\tilde{\mathbf{N}}^{kl})\Big|_{\mathbf{z}} \, \mathrm{d}z \\ &= 4 \int_{Z_{\frac{1}{2}s}} a_{ijkl} + a_{ijmn} e_{ymn}(\mathbf{N}^{kl})\Big|_{\mathbf{2z}} \, \mathrm{d}z \\ &= \frac{1}{4} \times 4 \int_{Y_s} a_{ijkl} + a_{ijmn} e_{ymn}(\mathbf{N}^{kl})\Big|_{\mathbf{y}} \, \mathrm{d}y \\ &= \int_{Y_s} a_{ijkl} + a_{ijmn} e_{ymn}(\mathbf{N}^{kl})\Big|_{\mathbf{y}} \, \mathrm{d}y. \end{aligned} \tag{C.10}$$

Comparing Eq. (C.10) with Eq. (17), we obtain $\tilde{C}_{ijkl} = C_{ijkl}$. Furthermore, according to Eq. (C.9), we obtain $\tilde{\mathbf{u}}^{(0)}(\mathbf{x}) = \mathbf{u}^{(0)}(\mathbf{x})$. Consequently, $\tilde{\mathbf{u}}^{2\epsilon}(\mathbf{x}) = \mathbf{u}^{\epsilon}(\mathbf{x})$ holds according to Eq. (C.7).

For arbitrary $k > 2, k \in \mathbb{N}$, a similar analysis procedure leads to $\tilde{\mathbf{u}}^{k\epsilon}(\mathbf{x}) = \mathbf{u}^{\epsilon}(\mathbf{x})$. Note that $\tilde{\mathbf{u}}^{k\epsilon}(\mathbf{x})$ and $\mathbf{u}^{\epsilon}(\mathbf{x})$ are both defined in the same periodic micro-structure. So the calculated average strain energy densities and energy release rate based on $\tilde{\mathbf{u}}^{k\epsilon}(\mathbf{x})$ must be the same for different k. This indicates that the fracture criterion is independent of RVE size $k\epsilon$.

References

Admal, N.C., Marian, J., Po, G., 2017. The atomistic representation of first strain-gradient elastic tensors. J. Mech. Phys. Solids 99, 93–115.

Aifantis, E.C., 1983. Dislocation kinetics and the formation of deformation bands. In: Sih, G.C., Provan, J.W. (Eds.), Defects Fracture and Fatigue. Martinus-Nijhoff, The Hague, pp. 75–84.
Aifantis, E., 2003. Update on a class of gradient theories. Mech. Mater. 35 (3), 259–280.
Bensoussan, A., Lions, J., Papanicolaou, G., 1978. Asymptotic Analysis for Periodic Structures. NorthHolland, Amsterdam.
Cao, L., Cui, J., 1999. Two-scale asymptotic analysis of fully periodic elastic structures of composite materials. J. Appl. Mech. 22 (1), 392.
Chen, J., Wei, Y., Huang, Y., Hutchinson, J., Hwang, K., 1999. The crack tip fields in strain gradient plasticity: the asymptotic and numerical analyses. Eng. Fract. Mech. 64 (5), 625–648.
Cioranescu, D., Donato, P., 1999. An Introduction to Homogenization. Oxford University Press.
Dascalu, C., Bilbie, G., Agiasofitou, E.K., 2008. Damage and size effects in elastic solids: A homogenization approach. Int. J. Solids Struct. 45 (2), 409–430.
Dong, H., Cui, J., Nie, Y., Yang, Z., 2018. Second-order two-scale computational method for damped dynamic thermo-mechanical problems of quasi-periodic composite materials. J. Comput. Appl. Math. 343, 575–601.
Drugan, W., 2000. Micromechanics-based variational estimates for a higher-order nonlocal constitutive equation and optimal choice of effective moduli for elastic composites. J. Mech. Phys. Solids 48 (6), 1359–1387.
Drugan, W., Willis, J., 1996. A micromechanics-based nonlocal constitutive equation and estimates of representative volume element size for elastic composites. J. Mech. Phys. Solids 44 (4), 497–524.
Eringen, A., 1972. Linear theory of nonlocal elasticity and dispersion of plane waves. Internat. J. Engrg. Sci. 10 (5), 425–435.
Eringen, A.C., 1974. Theory of nonlocal thermoelasticity. Int. J. Eng. Ence 12 (12), 1063–1077.
Fleck, N., Hutchinson, J., 1993. A phenomenological theory for strain gradient effects in plasticity. J. Mech. Phys. Solids 41 (12), 1825–1857.
Fleck, N.A., Hutchinson, J.W., 1997. Strain gradient plasticity. Adv. Appl. Mech. 33, 295–361.
Fleck, N., Hutchinson, J., 2001. A reformulation of strain gradient plasticity. J. Mech. Phys. Solids 49 (10), 2245–2271.
Forest, S., Pradel, F., Sab, K., 2001. Asymptotic analysis of heterogeneous cosserat media. Int. J. Solids Struct. 38 (26), 4585–4608.
Gao, H.H.Y.N.W., Hutchinson, J., 1999. Mechanism-based strain gradient plasticity-i. theory. J. Mech. Phys. Solids 47, 1239–1263.
Geers, M.G.D., Kouznetsova, V., Brekelmans, W.A.M., 2001. Gradient-enhanced computational homogenization for the micro-macro scale transition. J. Phys. IV 11 (PR5), 145–152.
Gei, M., Radi, E., 2003. Near-Tip Fields of Mode Iii Steady-State Crack Propagation in Elastic–Plastic Strain Gradient Solids. pp. 241–249.
Goutianos, S., 2011. Mode i and mixed mode crack-tip fields in strain gradient plasticity. Int. J. Non-Linear Mech. 46 (9), 1223–1231.
Gross, D., Seelig, T., 2018. Fracture mechanics: With an introduction to micromechanics.
Gudmundson, P., 2004. A unified treatment of strain gradient plasticity. J. Mech. Phys. Solids 52 (6), 1379–1406.
Gurtin, M.E., 2002. A gradient theory of single-crystal viscoplasticity that accounts for geometrically necessary dislocations. J. Mech. Phys. Solids 50 (1), 5–32.
Gutkin, M.Y., Aifantis, E.C., 2015. Dislocations and disclinations in gradient elasticity. Phys. Status Solidi 214 (2), 245–284.
Han, C.S., Gao, H., Huang, Y., Nix, W.D., 2004. Mechanism-based strain gradient crystal plasticity. J. Mech. Phys. Solids 821 (5), 1188–1203.
Han, F., Lubineau, G., Azdoud, Y., 2016. Adaptive coupling between damage mechanics and peridynamics: A route for objective simulation of material degradation up to complete failure. J. Mech. Phys. Solids 94, 453–472.
Jiang, H., Huang, Y., Zhuang, Z., Hwang, .K.C., 2001. Fracture in mechanism-based strain gradient plasticity. J. Mech. Phys. Solids 49 (5), 979–993.
Keita, O., Dascalu, C., Francois, B., 2014. A two-scale model for dynamic damage evolution. J. Mech. Phys. Solids 64 (mar), 170–183.
Kouznetsova, V., Geers, M.G.D., Brekelmans, W.A.M., 2002. Multi-scale constitutive modelling of heterogeneous materials with a gradient-enhanced computational homogenization scheme. Internat. J. Numer. Methods Engrg. 54 (8), 1235–1260.
Kuliev, V.D., Morozov, E.M., 2016. The gradient deformation criterion for brittle fracture. Doklady Phys. 61 (10), 502–504.
Lazar, M., Po, G., 2015. The non-singular green tensor of mindlin's anisotropic gradient elasticity with separable weak non-locality. Phys. Lett. A (379), 1538–1543.
Li, J., 2011. A micromechanics-based strain gradient damage model for fracture prediction of brittle materials - part i: Homogenization methodology and constitutive relations. Int. J. Solids Struct. 48 (24), 3336–3345.
Li, J., Pham, T., Abdelmoula, R., Song, F., Jiang, C., 2011. A micromechanics-based strain gradient damage model for fracture prediction of brittle materials - part ii: Damage modeling and numerical simulations. Int. J. Solids Struct. 48 (24), 3346–3358.
Li, J., Zhang, X.B., 2006. A criterion study for non-singular stress concentrations in brittle or quasi-brittle materials. Eng. Fract. Mech. 73 (4), 505–523.
Ma, Q., Cui, J., Li, Z., 2016. Second-order two-scale asymptotic analysis for axisymmetric and spherical symmetric structure with periodic configurations. Int. J. Solids Struct. s78–79, 77–100.
Martínez-Pañeda, E., Fleck, .N.A., 2019. Mode i crack tip fields: strain gradient plasticity theory versus j2 flow theory. Eur. J. Mech. A Solids 75, 381–388.
Menzel, A., 2000. On the continuum formulation of higher gradient plasticity for single and polycrystals. J. Mech. Phys. Solids 48 (8), 1777–1796.
Mindlin, R.D., 1965. Second gradient of strain and surface-tension in linear elasticity. Int. J. Solids Struct. 1 (4), 417–438.
Mindlin, R.D., Eshel, N.N., 1968. On first strain-gradient theories in linear elasticity. Int. J. Solids Struct. 4 (1), 109–124.
Nguyen, T.H., Niiranen, J., 2020. A second strain gradient damage model with a numerical implementation for quasi-brittle materials with micro-architectures:. Math. Mech. Solids 25 (3), 515–546.
Nix, W.D., Gao, H., 1998. Indentation size effects in crystalline materials: A law for strain gradient plasticity. J. Mech. Phys. Solids 46 (3), 411–425.
Oleinik, O., Shamaev, A., Yosifian, G., 1992. Mathematical Problems in Elasticity and Homogenization. NorthHolland, Amsterdam.
Peerlings, R.R., de, R. RenéBorst, Brekelmans, W.M., de Jhp, Henk Vree, 1996. Gradient enhanced damage for quasi-brittle materials. Internat. J. Numer. Methods Engrg. 39 (19), 3391–3403.
Peerlings, R.R., Fleck, N.N., 2004. Computational evaluation of strain gradient elasticity constants. Int. J. Multiscale Comput. Eng. 2 (4), 599–619.
Povstenko, Y.Z., 1999. The nonlocal theory of elasticity and its applications to the description of defects in solid bodies. J. Math. Sci. 97 (1), 3840–3845.
Ru, C.Q., Aifantis, E.C., 1993. A simple approach to solve boundary-value problems in gradient elasticity. Acta Mech. 101 (1–4), 59–68.
Silling, S.A., Epton, M., Weckner, O., Xu, J., Askari, E., 2007. Peridynamic states and constitutive modeling. J. Elasticity 88 (2), 151–184.
Smyshlyaev, V.P., Cherednichenko, K., 2000. On rigorous derivation of strain gradient effects in the overall behaviour of periodic heterogeneous media. J. Mech. Phys. Solids 48 (6), 1325–1357.
Sunyk, R., Steinmann, P., 2003. On higher gradients in continuum–atomistic modelling. Int. J. Solids Struct. 40 (24), 6877–6896.
Toupin, R., 1962. Elastic materials with couple-stresses. Arch. Ration. Mech. Anal. 11, 385–414.
Toupin, R., 1964. Theories of elasticity with couple-stress. Arch. Ration. Mech. Anal. 17, 85–112.
Triantafyllidis, N., Bardenhagen, S., 1996. The influence of scale size on the stability of periodic solids and the role of associated higher order gradient continuum models. J. Mech. Phys. Solids 44 (11), 1891–1928.
Xiang, M.Z., Cui, J.Z., Li, B.W., Tian, X., 2012. Atom-continuum coupled model for thermo-mechanical behavior of materials in micro-nano scales. Sci. China Phys. Mech. Astron. 55, 1125–1137.